

Supporting Information for "Projecting exposure to extreme climate impact events across six event categories and three spatial scales"

DOI: 10.1002/

Stefan Lange¹, Jan Volkholz¹, Tobias Geiger^{1,2}, Fang Zhao³, Iliusi Vega¹, Ted Veldkamp^{4,5}, Christopher P. O. Reyer¹, Lila Warszawski¹, Veronika Huber⁶, Jonas Jägermeyr^{1,7,8}, Jacob Schewe¹, David N. Bresch^{9,10}, Matthias Büchner¹, Jinfeng Chang^{5,11}, Philippe Ciais¹¹, Marie Dury¹², Kerry Emanuel¹³, Christian Folberth⁵, Dieter Gerten^{1,14}, Simon N. Gosling¹⁵, Manolis Grillakis¹⁶, Naota Hanasaki¹⁷, Alexandra-Jane Henrot¹², Thomas Hickler^{18,19}, Yasushi Honda²⁰, Akihiko Ito¹⁷, Nikolay Khabarov⁵, Aristeidis Koutroulis²¹, Wenfeng Liu^{11,22}, Christoph Müller¹, Kazuya Nishina¹⁷, Sebastian Ostberg¹, Hannes Müller Schmied^{18,19}, Sonia I. Seneviratne²³, Tobias Stacke²⁴, Jörg Steinkamp^{19,25}, Wim Thiery^{23,26}, Yoshihide Wada⁵, Sven Willner¹, Hong Yang^{22,27}, Minoru Yoshikawa²⁸, Chao Yue^{11,29}, and Katja Frieler¹

¹Potsdam Institute for Climate Impact Research (PIK), Member of the Leibniz Association, Potsdam, Germany

²Deutscher Wetterdienst (DWD), Climate and Environment Consultancy, Stahnsdorf, Germany

³School of Geographic Sciences, East China Normal University, Shanghai, China

⁴Institute for Environmental Studies, Vrije Universiteit Amsterdam, Amsterdam, Netherlands

⁵International Institute for Applied Systems Analysis (IIASA), Laxenburg, Austria

⁶Universidad Pablo de Olavide, Sevilla, Spain

⁷NASA Goddard Institute for Space Studies, New York, NY, USA

September 25, 2020, 3:14pm

⁸Department of Computer Science, University of Chicago, Chicago, IL, USA

⁹Institute for Environmental Decisions, ETH Zurich, Zurich, Switzerland

¹⁰Federal Office of Meteorology and Climatology MeteoSwiss, Zurich, Switzerland

¹¹Laboratoire des Sciences du Climat et de l'Environnement, CEA CNRS UVSQ, Institut Pierre Simon Laplace, Gif sur Yvette,
France

¹²Unit for Modelling of Climate and Biogeochemical Cycles, University of Liège, Liège, Belgium

¹³Lorenz Center, Massachusetts Institute of Technology, Cambridge, MA, USA

¹⁴Geography Department, Humboldt University of Berlin, Berlin, Germany

¹⁵School of Geography, University of Nottingham, Nottingham, UK

¹⁶Lab of Geophysical-Remote Sensing & Archaeo-environment, Institute for Mediterranean Studies, Rethymno, Greece

¹⁷National Institute for Environmental Studies, Tsukuba, Japan

¹⁸Institute of Physical Geography, Goethe University Frankfurt, Frankfurt, Germany

¹⁹Senckenberg Leibniz Biodiversity and Climate Research Centre (SBiK-F), Frankfurt, Germany

²⁰Faculty of Health and Sport Sciences, University of Tsukuba, Tsukuba, Japan

²¹Technical University of Crete, School of Environmental Engineering, Chania, Greece

²²Swiss Federal Institute of Aquatic Science and Technology (Eawag), Dübendorf, Switzerland

²³Institute for Atmospheric and Climate Science, ETH Zurich, Zurich, Switzerland

²⁴Institute of Coastal Research, Helmholtz-Zentrum Geesthacht, Geesthacht, Germany

²⁵Johannes Gutenberg-Universität Mainz, Mainz, Germany

²⁶Department of Hydrology and Hydraulic Engineering, Vrije Universiteit Brussel, Brussels, Belgium

²⁷Department of Environmental Sciences, MUG, University of Basel, Basel, Switzerland

²⁸Mizuho Information & Research Institute Inc., Tokyo, Japan

²⁹State Key Laboratory of Soil Erosion and Dryland Farming on the Loess Plateau, Northwest A&F University, Yangling, Shaanxi, China

Contents of this file

1. Text S1 to S6
2. Figures S1 to S20
3. Tables S1 to S5

Introduction The supporting texts describe details of our river flood simulations (Text S1), drought simulations (Text S2), wildfire simulations (Text S3), crop simulations (Text S4), tropical cyclone simulations (Text S5) and heatwave simulations (Text S6). The supporting figures show absolute and relative changes in global land area and population exposure to extremes from all six individual categories (Figs. S1–S6) and from aggregated categories (Figs. S7–S9), grid-level changes in land area and population exposure to extremes from all six categories (Figs. S10–S15), river flood protection levels according to the FLOPROS database (Fig. S16), and simulated and observed historical wildfire exposure at the grid level (Figs. S17–S20). The supporting tables list the main characteristics of our hydrological models (Table S1), crop models (Table S2), and wildfire models (Table S3), which direct human influences were considered in simulations with these models

Corresponding authors: S. Lange and K. Frieler, Potsdam Institute for Climate Impact Research (PIK), Telegrafenberg A56, 14473 Potsdam, Germany. (slange@pik-potsdam.de, katja.frieler@pik-potsdam.de)

(Table S4), and the GCM-specific number of simulation years per global warming level bin (Table S5).

Text S1. The global river model CaMa-Flood is used to translate daily runoff from the GHMs into daily discharge. For each GCM-GHM combination and at every grid cell, a Generalized Extreme Value (GEV) distribution (Jenkinson, 1955) is fitted to the preindustrial reference distribution of annual maximum discharge (up to 639 years worth of data) using L-moment estimators (Hosking & Wallis, 2005). The preindustrial reference samples used here are much larger than the 30 historical years often used in previous studies and allow for a more robust estimate of return periods. Since the preindustrial climate forcing could still contain biases, we use the frequency distribution of annual maximum daily discharge instead of flood depth and flooded area directly simulated by CaMa-Flood. Following the approach by Hirabayashi et al. (2013), annual maximum daily discharge with a return period of more than 100 years is mapped to a corresponding river flood depth from a retrospective CaMa-Flood run with MATSIRO (Takata et al., 2003) runoff, driven by observed climate forcing. To estimate the fraction of a $0.5^\circ \times 0.5^\circ$ grid cell that is exposed to the flood, the flood depth mapped to the retrospective MATSIRO run is then downscaled by CaMa-Flood based on high-resolution topography data (about 100 m spatial resolution) to yield the annual maximum flood inundation area fraction on a $2.5' \times 2.5'$ grid.

Text S2. The monthly soil moisture information used in this study that was provided by the individual GHMs refers to soil layers of different thicknesses (see Table S1). We use root moisture as directly provided by H08, MPI-HM, PCR-GLOBWB, and WaterGAP2. To approximate this variable for the other GHMs, we integrated soil moisture across the first seven soil layers of CLM45 (down to a depth of 78 cm), the first three layers of

JULES-W1 (down to a depth of 1 m), the first three layers of LPJmL (down to a depth of 1 m), and the first 9 layers of ORCHIDEE (down to a depth of 75 cm).

Text S3. CARAIB, LPJmL and LPJ-GUESS simulate a global land area exposed to wildfire in the 20th century ranging from 0.05 to 1.2 % per year while the global land area exposed to wildfire in the 20th century reaches about 5.5 % and even up to 8.5 % per year for some years for VISIT and ORCHIDEE, respectively. Hence, three GVMs underestimate and two overestimate the global land area exposed to wildfire compared to a reconstruction from a wide array of sources over the same period of about 4.0 % per year by Mouillot and Field (2005). As shown in Figs. S17–S20, this pattern remains the same when the simulated burned area is compared to three satellite-derived burned area datasets, namely GLOBCARBON (Plummer et al., 2007), L3JRC (Tansey et al., 2008) and GFED3.1 (Giglio et al., 2010). However, this comparison has to be interpreted with caution given that the satellite data only cover a short time period (2001–2005) and the climate data used to drive the GVM simulations during this time period do not correspond to the actual, observed climate.

The underestimation of burned area by three GVMs might be partly explained by an underestimation of fire return intervals in strongly fire-dominated ecosystem. (Mind that we compute the land area exposed to wildfire assuming fire return intervals of 1 year or longer.) However, we expect a more important factor to be the neglectance of GVMs to account for fire being intentionally or unintentionally used to clear natural vegetation as part of land-use changes. Even though the reconstruction by Mouillot and Field (2005) does not account for burning of agricultural wastes, nor for prescribed burning as part of landscape clearing or deforestation, overall, it does account for a wider range of fires

than considered by the GVMs such as fires escaping from agricultural lands and during land clearing (as long as these have been reported by firefighters). Additionally, there are model-specific reasons for an underestimation of burned area: CARAIB only considers natural ignitions from lightning and the fire module parameters are uncalibrated, i.e. have not been adjusted to observed burned area. LPJmL underestimates fire occurrence in savannah regions due to a lack of human ignitions and also defines rangelands and other extensively managed grasslands as pastures that cannot burn. LPJ-GUESS, despite allowing fire to occur on croplands and pastures, features a rather small burned area. LPJ-GUESS has been found to be very sensitive to the choice of the fire module (Andela et al., 2017) and the fire module used in this study (GlobFIRM; Thonicke et al., 2001) is known to underestimate burned area, since at the time it was developed estimates of burned area were lower (Giglio et al., 2013) and GlobFIRM was calibrated with data on fire return intervals rather than burned area (Thonicke et al., 2001).

The reasons for overestimating the global burned area are also model specific. One reason might be that ORCHIDEE and VISIT are the only GVMs in our ensemble that do not simulate dynamic vegetation, which might lead to increasing maladaptation of regrowing vegetation after a fire to climate change-induced changes in fire risk. Additionally, the overestimation of fire in boreal regions and in Northern China/India and several other regions due to a lack of fire suppression in VISIT is known to outweigh the underestimation of fire in savannah regions due to lacking human ignitions (Kato et al., 2013). ORCHIDEE overestimates global burned area also because of the large grassland and pasture fraction available to burn and a lower tree fraction as compared to previous burned area evaluations of the model (Yue et al., 2014). In ORCHIDEE, the fire spread rate is

inversely linked with the fuel bulk density. Grassland have a low fuel bulk density (more loosely packed fuel) so a higher grassland fraction leads to lower fuel bulk density and a high spread rate, which leads to higher burned area. Another reason for the difference between the burned area simulations of ORCHIDEE in this study and the ORCHIDEE model evaluation study presented in Yue et al. (2014) could be the different climate input data used.

Text S4. When calculating population exposure to crop failure we only account for local effects on people working in agriculture. Large-scale market effects cannot be captured here with biophysical impact models. Also, we argue that most crop failure events are too small-scale to significantly affect consumers thanks to buffering by the market.

If fraction A_{failure} of the land area of a grid cell is exposed to crop failure, then the exposed population fraction of that grid cell, P_{failure} , is calculated according to

$$P_{\text{failure}} = F \frac{A_{\text{failure}}}{A_{\text{agriculture}}},$$

where F is national employment in agriculture as a fraction of total employment and $A_{\text{agriculture}}$ is the land area fraction of the grid cell used for agriculture. The factor $A_{\text{failure}}/A_{\text{agriculture}}$ is supposed to estimate the fraction of the local population working in agriculture that is exposed to the crop failure. This factor is smaller than one if not all of the crops grown in the grid cell failed. Values for F are taken from the World Development Indicators (2017). Gaps in the national time series of employment in agriculture are filled by linear interpolation and the fraction is assumed to stay constant before the first and the last available data point.

Text S5. For every year we generate 100 realizations of tropical cyclone (TC) tracks and consider every realization as equivalent to the output of one TC impact model. For the

historical period and the RCP scenarios, a global total of 300 potential TC tracks per year as well as the expected number of cyclones for each year are generated based on GCM output. Let N be the expected number of TCs for an arbitrary but fixed year. We then generate 100 TC track realizations by drawing 100 random samples of size N from the 300 potential TC tracks of that year.

The approach differs somewhat for the preindustrial baseline scenario because in this case (i) there are only 100 potential TC tracks available per year and (ii) the underlying GCM years do not necessarily match the years used by all other impact models. To generate a sample of 100 potential realizations of TC tracks that correspond to the years used by the other impact models, we select at least three years of TC simulations that match a year used by the other impact models in terms of the low frequency variability of global mean temperature (GMT; 21-year running-mean) and the 3-month running-mean of the Equatorial Southern Oscillation Index (ESOI; as defined by NOAA's Climate Prediction Center; see <http://www.cpc.ncep.noaa.gov/data/indices/>). The algorithm initially sets a very strong threshold of similarity and iteratively and alternatively for GMT and ESOI lowers the threshold until at least three years have been selected. In this way we create a sample of at least 300 TCs we can draw from. The expected number of TCs to draw is randomly selected from the expected numbers of cyclones associated with the years contributing to the sample. As both GMT and ESOI (or variants thereof) have been shown to significantly modulate the occurrence of climate extremes, see e.g. Frank and Young (2007) and Ward et al. (2014), we thereby account for relevant regional climate extreme patterns within this and across extreme event categories.

A special case is HadGEM2-ES as for this GCM, TC tracks are neither available for the preindustrial baseline scenario nor for the historical period 1861–1949. In order to still provide results for this GCM, the missing data are filled by repeated copies of data from the historical period 1950–1979, which is characterized by approximately stationary global mean temperature for HadGEM2-ES.

Text S6. A grid cell is considered to be exposed to a heatwave in a given year if (i) the Heat Wave Magnitude Index daily (HWMId) of that year exceeds the 97.5th percentile of the HWMId distribution under preindustrial climate conditions of that grid cell and (ii) the Humidex exceeds a value of 45 on all days of the hot period corresponding to the HWMId value of the given year.

The HWMId is defined as the maximum magnitude of all hot periods occurring in a year, where a hot period is a period of at least 3 consecutive days with daily maximum temperature exceeding a threshold value $T_{\text{pi}90}$ which is defined as the 90th percentile of daily maximum temperatures under preindustrial climate conditions, centered on a 31-day window. The magnitude of each hot period in a year is the sum of the daily magnitudes on the consecutive days composing the hot period, with daily magnitude calculated according to $M_d(T_d) = 0$ if $T_d \leq T_{\text{pi}25}$ else $(T_d - T_{\text{pi}25}) / (T_{\text{pi}75} - T_{\text{pi}25})$, where T_d is the daily maximum temperature on day d of the hot period and $T_{\text{pi}25}$ and $T_{\text{pi}75}$ are the 25th and 75th percentile, respectively, of the annual maximum of the daily maximum temperature under preindustrial climate conditions. In order to estimate $T_{\text{pi}90}$, $T_{\text{pi}25}$, and $T_{\text{pi}75}$, we use more than 400 years of daily maximum temperature data of 0.5 spatial resolution representing preindustrial climate conditions as available from the ISIMIP2b climate input data set (Frieler et al., 2017). Based on these more than 400 years of

temperature data we then derive the 97.5th percentile of the HWMI distribution under preindustrial climate conditions.

The Humidex was developed to capture the experienced effects of hot weather on the human body by combining temperature and relative humidity via the dew point to an effective temperature. We use the Humidex definition by Environment Canada (https://climate.weather.gc.ca/glossary_e.html#h) and calculate the index at the time of maximum daily temperature, according to

$$\text{Humidex} = T_{\max} + \frac{5}{9} \left\{ 6.11 \exp \left[5417.7530 \left(\frac{1}{273.16} - \frac{1}{273.15 + T_{\text{dew}}} \right) \right] - 10 \right\},$$

where T_{\max} is the daily maximum temperature and T_{dew} is the dew point at the time of maximum daily temperature, which we approximately compute using daily mean temperature and relative humidity, exploiting that the dew point does usually not vary much over the course of a day (Pierce, 1934; Schwartzman et al., 1998). We use a Humidex threshold value of 45 because the Canadian Center for Occupational Health and Safety (CCOHS, 2017) links the Humidex to stress on the human body using the categories *comfortable* (for values between 20 and 29), *some discomfort* (30–39), *great discomfort, avoid exertion* (40–45), and *dangerous, heat stroke possible* (above 45).

References

- Andela, N., Morton, D. C., Giglio, L., Chen, Y., van der Werf, G. R., Kasibhatla, P. S., ... Randerson, J. T. (2017). A human-driven decline in global burned area. *Science*, 356(6345), 1356–1362. doi: 10.1126/science.aal4108
- Best, M. J., Pryor, M., Clark, D. B., Rooney, G. G., Essery, R. L. H., Ménard, C. B., ... Harding, R. J. (2011). The Joint UK Land Environment Simulator (JULES), model

description Part 1: Energy and water fluxes. *Geoscientific Model Development*, 4(3), 677–699. doi: 10.5194/gmd-4-677-2011

Bondeau, A., Smith, P. C., Zaehle, S., Schaphoff, S., Lucht, W., Cramer, W., ... Smith, B. (2007). Modelling the role of agriculture for the 20th century global terrestrial carbon balance. *Global Change Biology*, 13(3), 679–706. doi: 10.1111/j.1365-2486.2006.01305.x

CCOHS. (2017). *Humidex Rating and Work*. Retrieved from https://www.ccohs.ca/oshanswers/phys_agents/humidex.html (Access date: 27 October 2017)

Dury, M., Hambuckers, A., Warnant, P., Henrot, A., Favre, E., Ouberdous, M., & François, L. (2011). Responses of European forest ecosystems to 21st century climate: assessing changes in interannual variability and fire intensity. *iForest - Biogeosciences and Forestry*, 4, 82–99. doi: 10.3832/ifor0572-004

Elliott, J., Müller, C., Deryng, D., Chryssanthacopoulos, J., Boote, K. J., Büchner, M., ... Sheffield, J. (2015). The Global Gridded Crop Model Intercomparison: data and modeling protocols for Phase 1 (v1.0). *Geoscientific Model Development*, 8(2), 261–277. doi: 10.5194/gmd-8-261-2015

Folberth, C., Elliott, J., Müller, C., Balkovic, J., Chryssanthacopoulos, J., Izaurrealde, R. C., ... Wang, X. (2016). Uncertainties in global crop model frameworks: effects of cultivar distribution, crop management and soil handling on crop yield estimates. *Biogeosciences Discussions*, 2016, 1–30. doi: 10.5194/bg-2016-527

Folberth, C., Gaiser, T., Abbaspour, K. C., Schulín, R., & Yang, H. (2012). Regionalization of a large-scale crop growth model for sub-Saharan Africa: Model setup, evaluation, and estimation of maize yields. *Agriculture, Ecosystems & Environment*,

151, 21–33. doi: 10.1016/j.agee.2012.01.026

Frank, W. M., & Young, G. S. (2007). The Interannual Variability of Tropical Cyclones.

Monthly Weather Review, 135(10), 3587–3598. doi: 10.1175/MWR3435.1

Frieler, K., Lange, S., Piontek, F., Reyer, C. P. O., Schewe, J., Warszawski, L., ...

Yamagata, Y. (2017). Assessing the impacts of 1.5 °C global warming – simulation protocol of the Inter-Sectoral Impact Model Intercomparison Project (ISIMIP2b).

Geoscientific Model Development, 10(12), 4321–4345. doi: 10.5194/gmd-10-4321-2017

Giglio, L., Randerson, J. T., & van der Werf, G. R. (2013). Analysis of daily, monthly,

and annual burned area using the fourth-generation global fire emissions database (GFED4). *Journal of Geophysical Research: Biogeosciences*, 118(1), 317–328. doi:

10.1002/jgrg.20042

Giglio, L., Randerson, J. T., van der Werf, G. R., Kasibhatla, P. S., Collatz, G. J.,

Morton, D. C., & DeFries, R. S. (2010). Assessing variability and long-term trends in burned area by merging multiple satellite fire products. *Biogeosciences*, 7(3),

1171–1186. doi: 10.5194/bg-7-1171-2010

Guimberteau, M., Ducharne, A., Ciais, P., Boisier, J. P., Peng, S., De Weirtdt, M., &

Verbeeck, H. (2014). Testing conceptual and physically based soil hydrology schemes against observations for the Amazon Basin. *Geoscientific Model Development*, 7(3),

1115–1136. doi: 10.5194/gmd-7-1115-2014

Hagemann, S., & Dümenil Gates, L. (2003). Improving a subgrid runoff parameterization

scheme for climate models by the use of high resolution data derived from satellite observations. *Climate Dynamics*, 21(3–4), 349–359. doi: 10.1007/s00382-003-0349-x

- Hanasaki, N., Yoshikawa, S., Pokhrel, Y., & Kanae, S. (2018). A global hydrological simulation to specify the sources of water used by humans. *Hydrology and Earth System Sciences*, 22(1), 789–817. doi: 10.5194/hess-22-789-2018
- Hirabayashi, Y., Mahendran, R., Koirala, S., Konoshima, L., Yamazaki, D., Watanabe, S., ... Kanae, S. (2013). Global flood risk under climate change. *Nature Climate Change*, 3(9), 816–821. doi: 10.1038/nclimate1911
- Hosking, J., & Wallis, J. (2005). *Regional Frequency Analysis: An Approach Based on L-Moments*. Cambridge University Press.
- Ito, A., & Inatomi, M. (2012). Water-Use Efficiency of the Terrestrial Biosphere: A Model Analysis Focusing on Interactions between the Global Carbon and Water Cycles. *Journal of Hydrometeorology*, 13(2), 681–694. doi: 10.1175/JHM-D-10-05034.1
- Ito, A., & Oikawa, T. (2002). A simulation model of the carbon cycle in land ecosystems (Sim-CYCLE): a description based on dry-matter production theory and plot-scale validation. *Ecological Modelling*, 151(2), 143–176. doi: 10.1016/S0304-3800(01)00473-2
- Jenkinson, A. F. (1955). The frequency distribution of the annual maximum (or minimum) values of meteorological elements. *Quarterly Journal of the Royal Meteorological Society*, 81(348), 158–171. doi: 10.1002/qj.49708134804
- Kato, E., Kinoshita, T., Ito, A., Kawamiya, M., & Yamagata, Y. (2013). Evaluation of spatially explicit emission scenario of land-use change and biomass burning using a process-based biogeochemical model. *Journal of Land Use Science*, 8(1), 104–122. doi: 10.1080/1747423X.2011.628705
- Klein Goldewijk, K., Beusen, A., Doelman, J., & Stehfest, E. (2017). Anthropogenic

land use estimates for the Holocene – HYDE 3.2. *Earth System Science Data*, 9(2), 927–953. doi: 10.5194/essd-9-927-2017

Lawrence, D. M., Oleson, K. W., Flanner, M. G., Thornton, P. E., Swenson, S. C., Lawrence, P. J., ... Slater, A. G. (2011). Parameterization improvements and functional and structural advances in Version 4 of the Community Land Model. *Journal of Advances in Modeling Earth Systems*, 3(1). (M03001) doi: 10.1029/2011MS00045

Liu, W., Yang, H., Folberth, C., Wang, X., Luo, Q., & Schulín, R. (2016). Global investigation of impacts of PET methods on simulating crop-water relations for maize. *Agricultural and Forest Meteorology*, 221, 164–175. doi: 10.1016/j.agrformet.2016.02.017

Liu, W., Yang, H., Liu, J., Azevedo, L. B., Wang, X., Xu, Z., ... Schulín, R. (2016). Global assessment of nitrogen losses and trade-offs with yields from major crop cultivations. *Science of The Total Environment*, 572, 526–537. doi: 10.1016/j.scitotenv.2016.08.093

Mouillot, F., & Field, C. B. (2005). Fire history and the global carbon budget: a $1^\circ \times 1^\circ$ fire history reconstruction for the 20th century. *Global Change Biology*, 11(3), 398–420. doi: 10.1111/j.1365-2486.2005.00920.x

Müller, C., Elliott, J., Chrysanthacopoulos, J., Arneth, A., Balkovic, J., Ciais, P., ... Yang, H. (2017). Global gridded crop model evaluation: benchmarking, skills, deficiencies and implications. *Geoscientific Model Development*, 10(4), 1403–1422. doi: 10.5194/gmd-10-1403-2017

Müller Schmied, H., Adam, L., Eisner, S., Fink, G., Flörke, M., Kim, H., ... Döll, P. (2016). Variations of global and continental water balance components as impacted

- by climate forcing uncertainty and human water use. *Hydrology and Earth System Sciences*, 20(7), 2877–2898. doi: 10.5194/hess-20-2877-2016
- Müller Schmied, H., Eisner, S., Franz, D., Wattenbach, M., Portmann, F. T., Flörke, M., & Döll, P. (2014). Sensitivity of simulated global-scale freshwater fluxes and storages to input data, hydrological model structure, human water use and calibration. *Hydrology and Earth System Sciences*, 18(9), 3511–3538. doi: 10.5194/hess-18-3511-2014
- Oleson, K. W., Lawrence, D. M., Bonan, G. B., Drewniak, B., Huang, M., Koven, C. D., ... Yang, Z.-L. (2013). *Technical Description of version 4.5 of the Community Land Model (CLM)* (Tech. Rep. Nos. NCAR/TN-503+STR). NCAR Technical Note. doi: 10.5065/D6RR1W7M
- Papadimitriou, L. V., Koutroulis, A. G., Grillakis, M. G., & Tsanis, I. K. (2017). The effect of GCM biases on global runoff simulations of a land surface model. *Hydrology and Earth System Sciences*, 21(9), 4379–4401. doi: 10.5194/hess-21-4379-2017
- Pierce, L. T. (1934). Diurnal Variation in the Dew-Point Temperature at Asheville, N. C. *Monthly Weather Review*, 62(8), 289–293. doi: 10.1175/1520-0493(1934)62<289:DVITDT>2.0.CO;2
- Plummer, S., Arino, O., Ranera, F., Tansey, K., Chen, J., Dedieu, G., ... McCallum, I. (2007). An Update on the globcarbon initiative: multi-sensor estimation of global biophysical products for global terrestrial carbon studies. In *Proceedings of Envisat Symposium 2007, 23–27 April 2007, Montreux, Switzerland*. ESA Communication Production Office, ESTEC. Retrieved from <http://eprints.ucl.ac.uk/179082/>
- Rost, S., Gerten, D., Bondeau, A., Lucht, W., Rohwer, J., & Schaphoff, S. (2008).

- Agricultural green and blue water consumption and its influence on the global water system. *Water Resources Research*, 44(9), 1–17. doi: 10.1029/2007WR006331
- Sacks, W. J., Deryng, D., Foley, J. A., & Ramankutty, N. (2010). Crop planting dates: an analysis of global patterns. *Global Ecology and Biogeography*, 19(5), 607–620. doi: 10.1111/j.1466-8238.2010.00551.x
- Schaphoff, S., Heyder, U., Ostberg, S., Gerten, D., Heinke, J., & Lucht, W. (2013). Contribution of permafrost soils to the global carbon budget. *Environmental Research Letters*, 8(1), 014026. doi: 10.1088/1748-9326/8/1/014026
- Schwartzman, P. D., Michaels, P. J., & Knappenberger, P. C. (1998). Observed changes in the diurnal dewpoint cycles across North America. *Geophysical Research Letters*, 25(13), 2265–2268. doi: 10.1029/98GL01843
- Scussolini, P., Aerts, J. C. J. H., Jongman, B., Bouwer, L. M., Winsemius, H. C., deMoel, H., & Ward, P. J. (2016). FLOPROS: an evolving global database of flood protection standards. *Natural Hazards and Earth System Sciences*, 16(5), 1049–1061. doi: 10.5194/nhess-16-1049-2016
- Smith, B., Wårlind, D., Arneth, A., Hickler, T., Leadley, P., Siltberg, J., & Zaehle, S. (2014). Implications of incorporating N cycling and N limitations on primary production in an individual-based dynamic vegetation model. *Biogeosciences*, 11(7), 2027–2054. doi: 10.5194/bg-11-2027-2014
- Stacke, T., & Hagemann, S. (2012). Development and validation of a global dynamical wetlands extent scheme. *Hydrology and Earth System Sciences Discussions*, 9(1), 405–440. doi: 10.5194/hessd-9-405-2012
- Stehfest, E., Heistermann, M., Priess, J. A., Ojima, D. S., & Alcamo, J. (2007). Sim-

- ulation of global crop production with the ecosystem model DayCent. *Ecological Modelling*, 209(2), 203–219. doi: 10.1016/j.ecolmodel.2007.06.028
- Takata, K., Emori, S., & Watanabe, T. (2003). Development of the minimal advanced treatments of surface interaction and runoff. *Global and Planetary Change*, 38(1), 209–222. (Project for Intercomparison of Land-surface Parameterization Schemes, Phase 2(e)) doi: 10.1016/S0921-8181(03)00030-4
- Tansey, K., Grégoire, J.-M., Defourny, P., Leigh, R., Pekel, J.-F., van Bogaert, E., & Bartholomé, E. (2008). A new, global, multi-annual (2000–2007) burnt area product at 1 km resolution. *Geophysical Research Letters*, 35(1). (L01401) doi: 10.1029/2007GL031567
- Thonicke, K., Spessa, A., Prentice, I. C., Harrison, S. P., Dong, L., & Carmona-Moreno, C. (2010). The influence of vegetation, fire spread and fire behaviour on biomass burning and trace gas emissions: results from a process-based model. *Biogeosciences*, 7(6), 1991–2011. doi: 10.5194/bg-7-1991-2010
- Thonicke, K., Venevsky, S., Sitch, S., & Cramer, W. (2001). The role of fire disturbance for global vegetation dynamics: coupling fire into a Dynamic Global Vegetation Model. *Global Ecology and Biogeography*, 10(6), 661–677. doi: 10.1046/j.1466-822X.2001.00175.x
- Wada, Y., de Graaf, I. E. M., & van Beek, L. P. H. (2016). High-resolution modeling of human and climate impacts on global water resources. *Journal of Advances in Modeling Earth Systems*, 8(2), 735–763. doi: 10.1002/2015MS000618
- Wada, Y., Wisser, D., & Bierkens, M. F. P. (2014). Global modeling of withdrawal, allocation and consumptive use of surface water and groundwater resources. *Earth*

- System Dynamics*, 5(1), 15–40. doi: 10.5194/esd-5-15-2014
- Ward, P. J., Jongman, B., Kumm, M., Dettinger, M. D., Sperna Weiland, F. C., & Winsemius, H. C. (2014). Strong influence of El Niño Southern Oscillation on flood risk around the world. *Proceedings of the National Academy of Sciences*, 111(44), 15659–15664. doi: 10.1073/pnas.1409822111
- Williams, J. (1995). The EPIC Model [Book Section]. In V. P. Singh (Ed.), *Computer models of watershed hydrology* (p. 909-1000). Littleton, USA: Water Resources Publications.
- World Development Indicators. (2017). *Employment in agriculture (percent of total employment) (modeled ILO estimate)*. Retrieved from <https://data.worldbank.org/indicator/SL.AGR.EMPL.ZS>
- Yue, C., Ciais, P., Cadule, P., Thonicke, K., Archibald, S., Poulter, B., ... Viovy, N. (2014). Modelling the role of fires in the terrestrial carbon balance by incorporating SPITFIRE into the global vegetation model ORCHIDEE – Part 1: simulating historical global burned area and fire regimes. *Geoscientific Model Development*, 7(6), 2747–2767. doi: 10.5194/gmd-7-2747-2014
- Yue, C., Ciais, P., Cadule, P., Thonicke, K., & van Leeuwen, T. T. (2015). Modelling the role of fires in the terrestrial carbon balance by incorporating SPITFIRE into the global vegetation model ORCHIDEE – Part 2: Carbon emissions and the role of fires in the global carbon balance. *Geoscientific Model Development*, 8(5), 1321–1338. doi: 10.5194/gmd-8-1321-2015

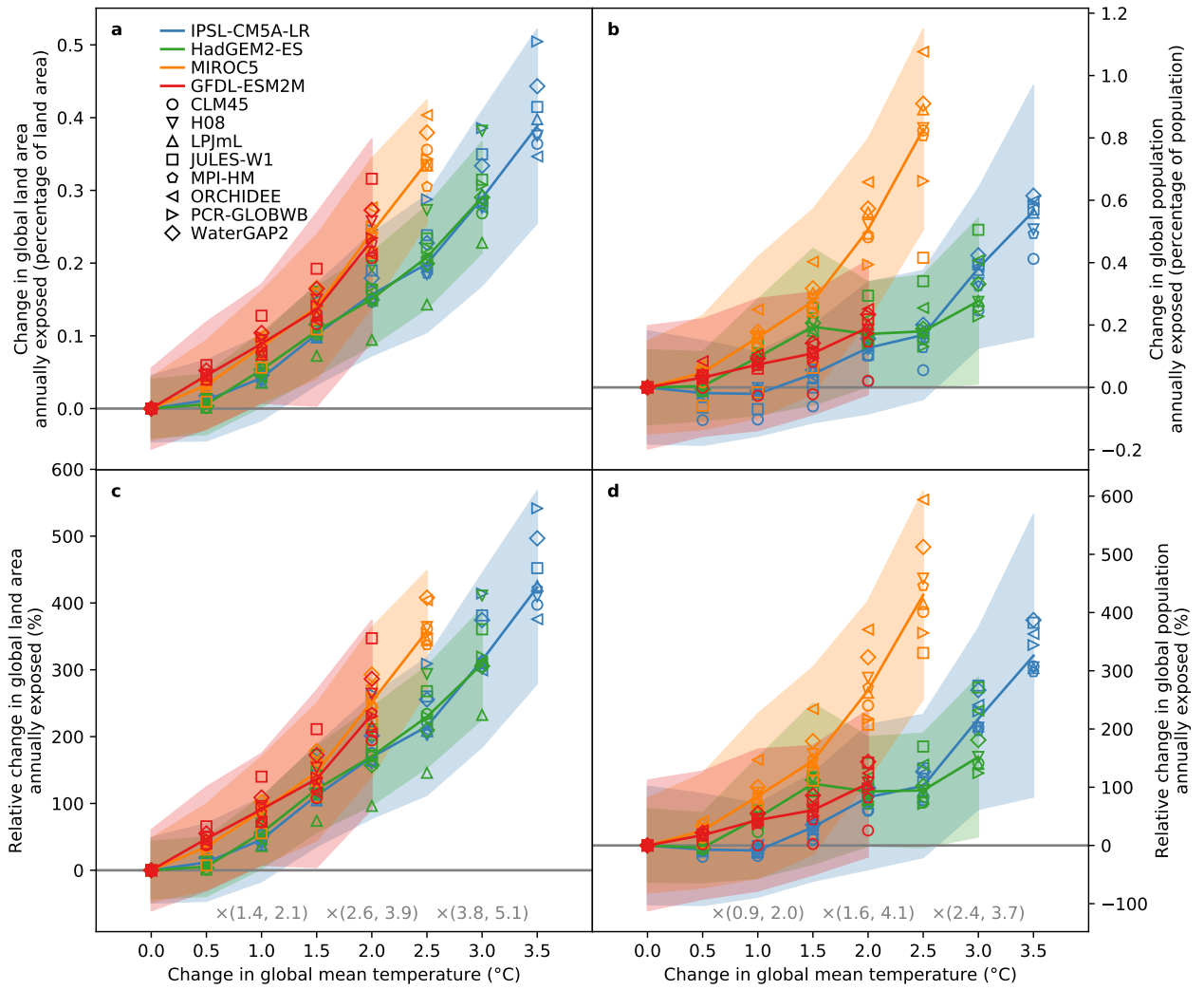


Figure S1. Pure effect of climate change on global (left) land area and (right) population annually exposed to river floods. Shown are (top) changes and (bottom) relative changes in global exposure at different levels of global mean temperature change relative to the preindustrial baseline. Symbols indicate multi-year mean changes for each GHM (symbol) and GCM (color). Lines represent medians over all GHMs per GCM. Shaded areas represent the multi-GHM median of the multi-year mean change in exposure \pm the multi-GHM median of the interannual standard deviation of exposure. Grey numbers at the bottom of panels c–d indicate the central 90 % multi-model range of change factors at 1°C, 2°C, and 3°C global warming relative to preindustrial conditions.

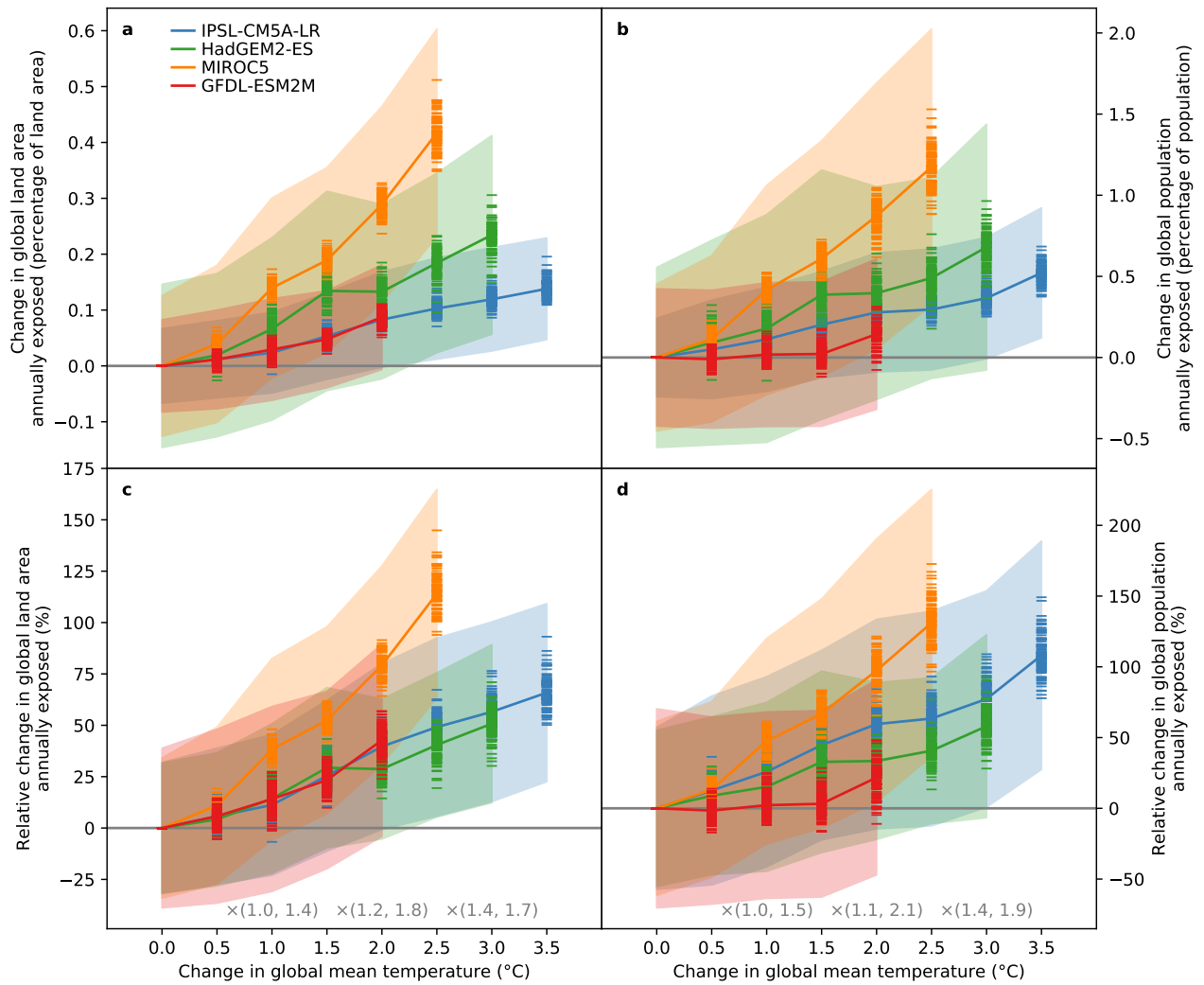


Figure S2. Pure effect of climate change on global (left) land area and (right) population annually exposed to tropical cyclones. Shown are (top) changes and (bottom) relative changes in global exposure at different levels of global mean temperature change relative to the preindustrial baseline. Bars indicate multi-year mean changes for each GCM (color) and tropical cyclone track realization. Lines represent medians over all realizations per GCM. Shaded areas represent the multi-realization median of the multi-year mean change in exposure \pm the multi-realization median of the interannual standard deviation of exposure. Grey numbers at the bottom of panels c–d indicate the central 90% multi-model range of change factors at 1 °C, 2 °C, and 3 °C global warming relative to preindustrial conditions.

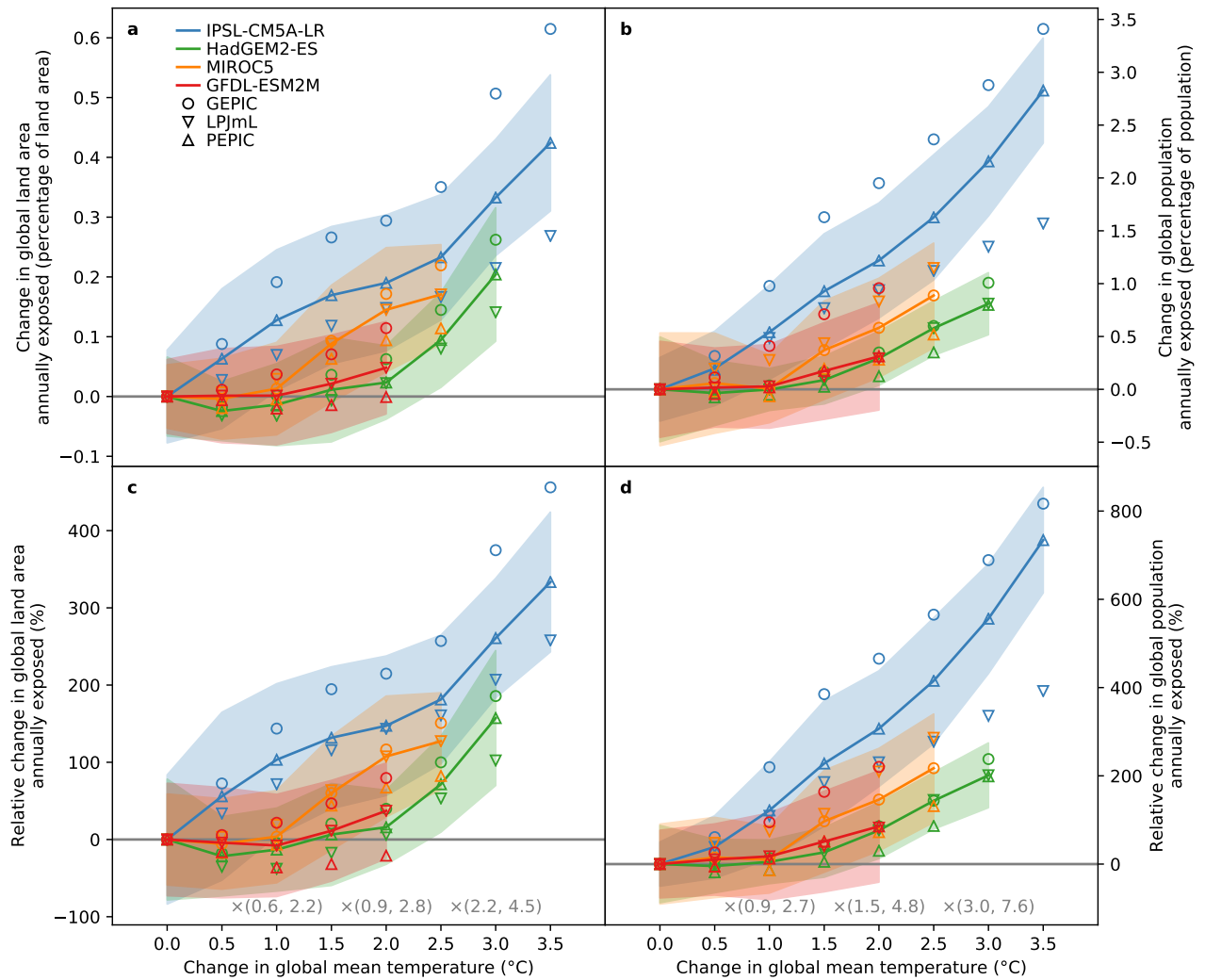


Figure S3. Same as Fig. S1 but for global exposure to crop failure.

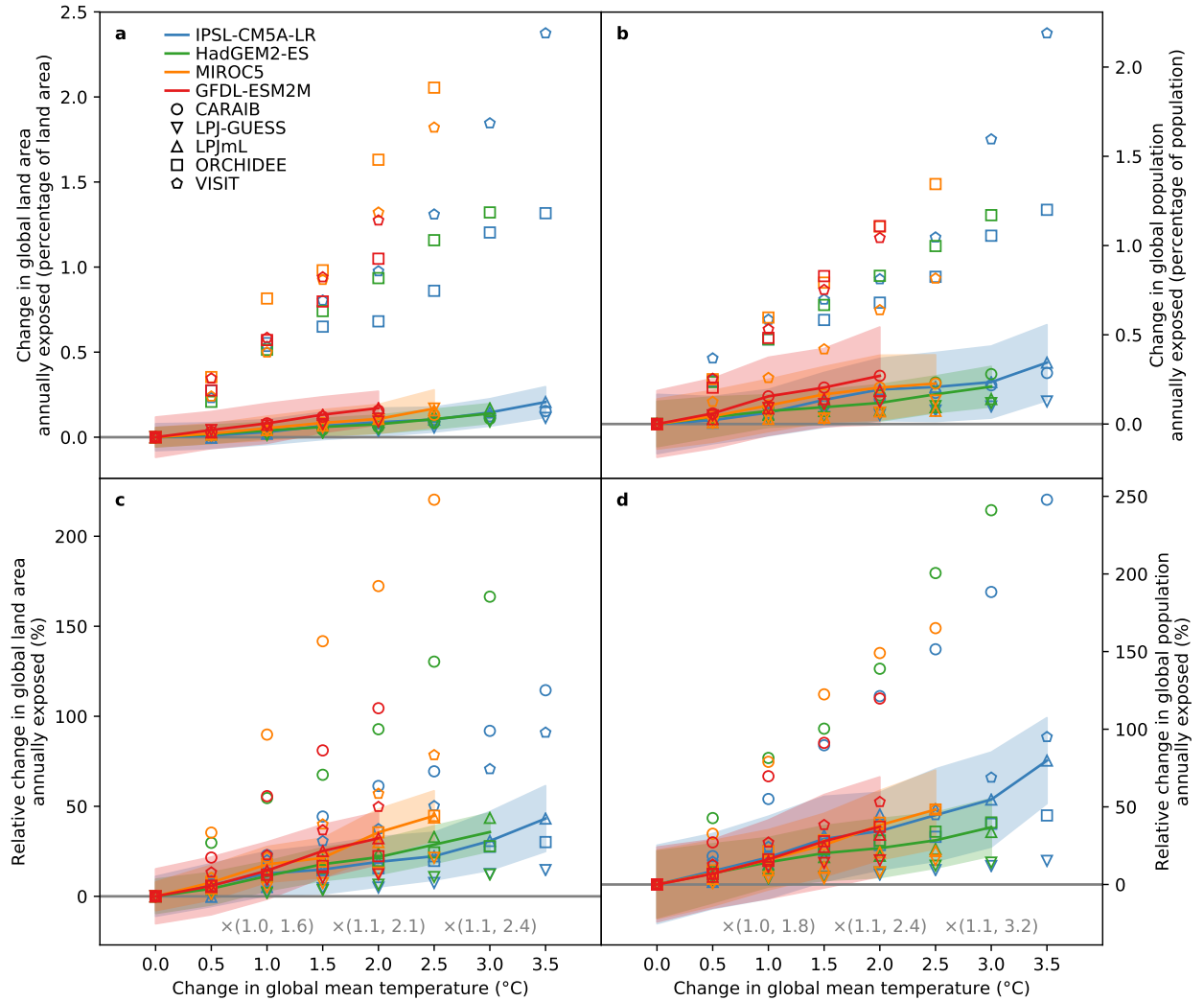


Figure S4. Same as Fig. S1 but for global exposure to wildfires.

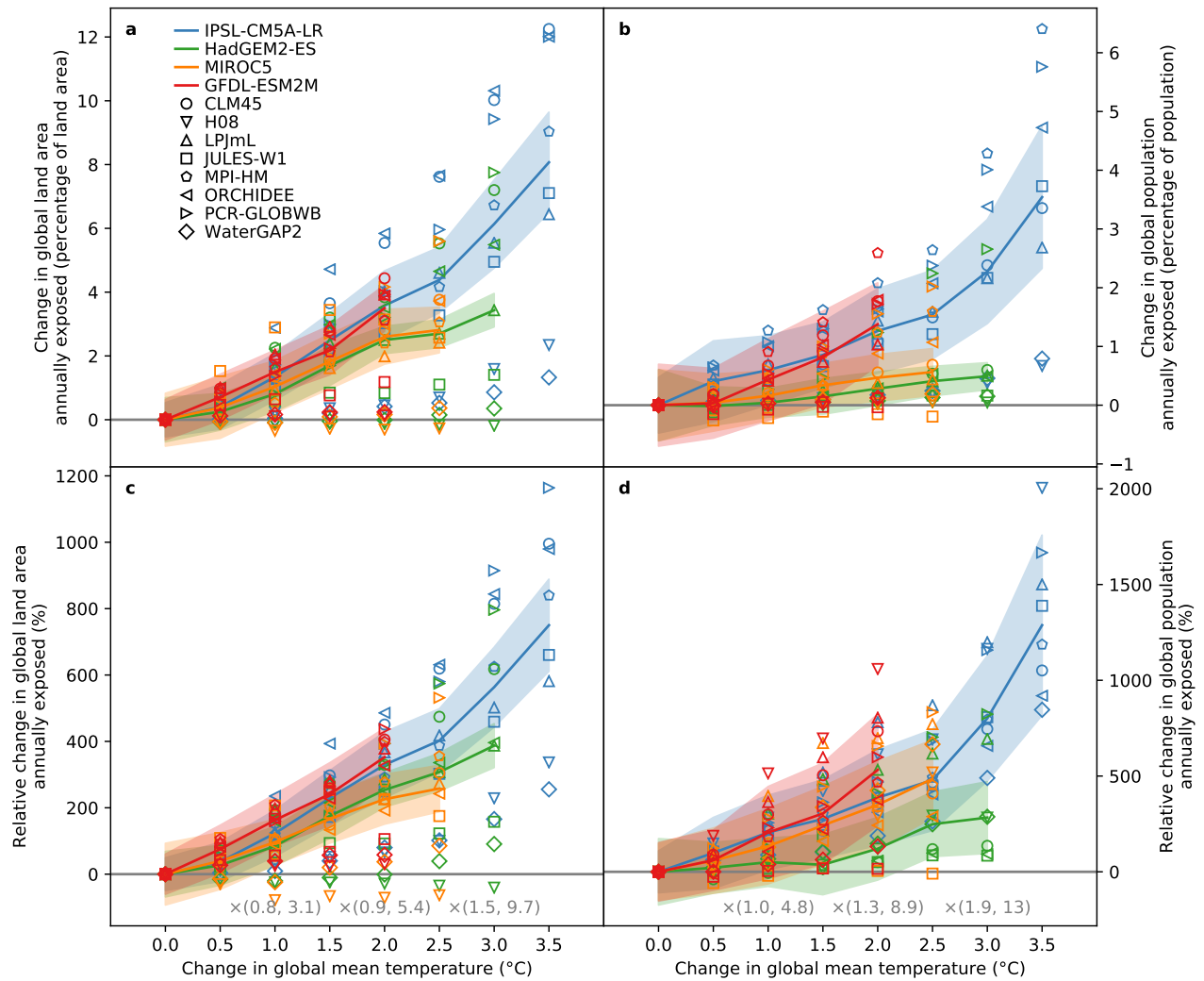


Figure S5. Same as Fig. S1 but for global exposure to droughts.

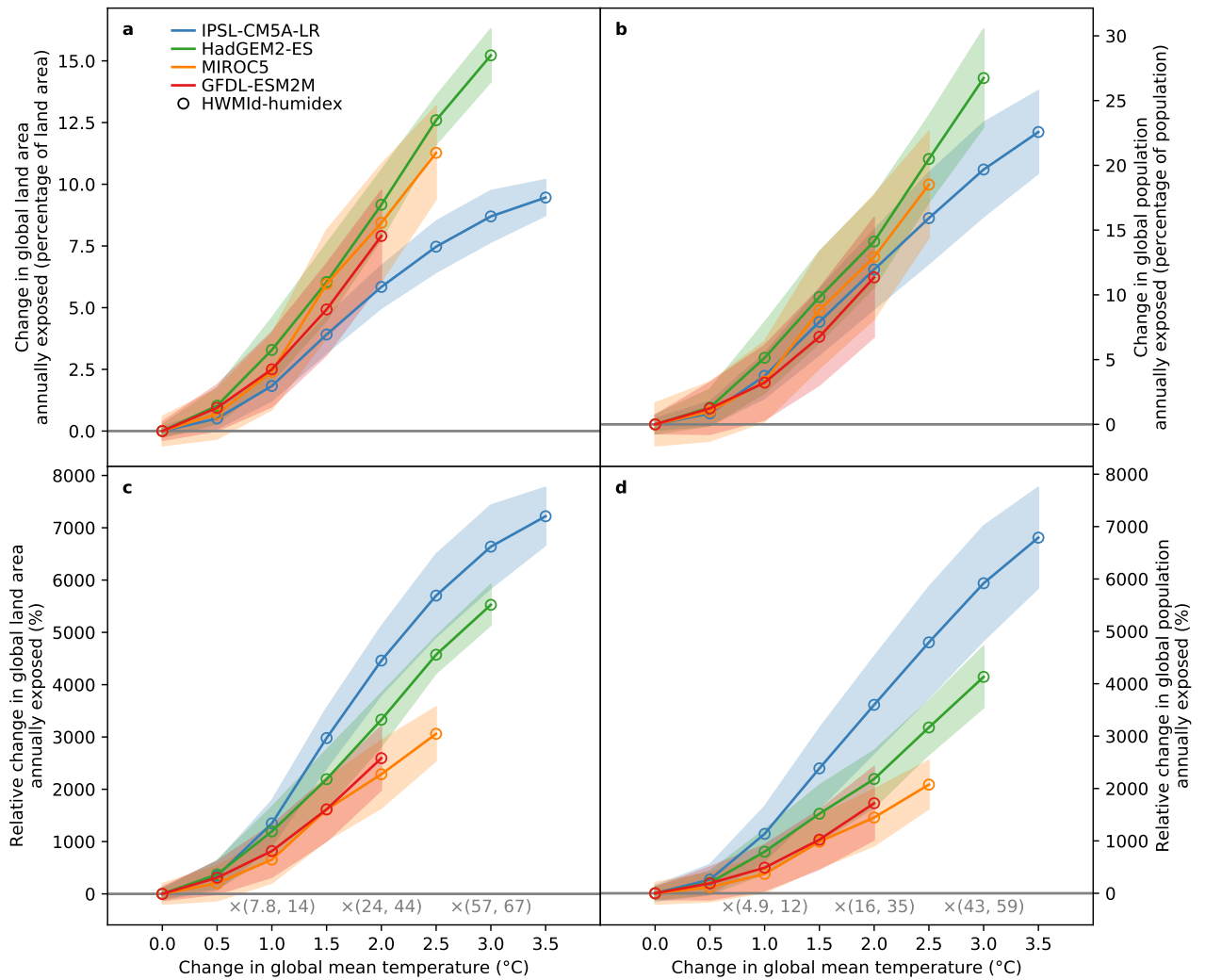


Figure S6. Same as Fig. S1 but for global exposure to heatwaves.

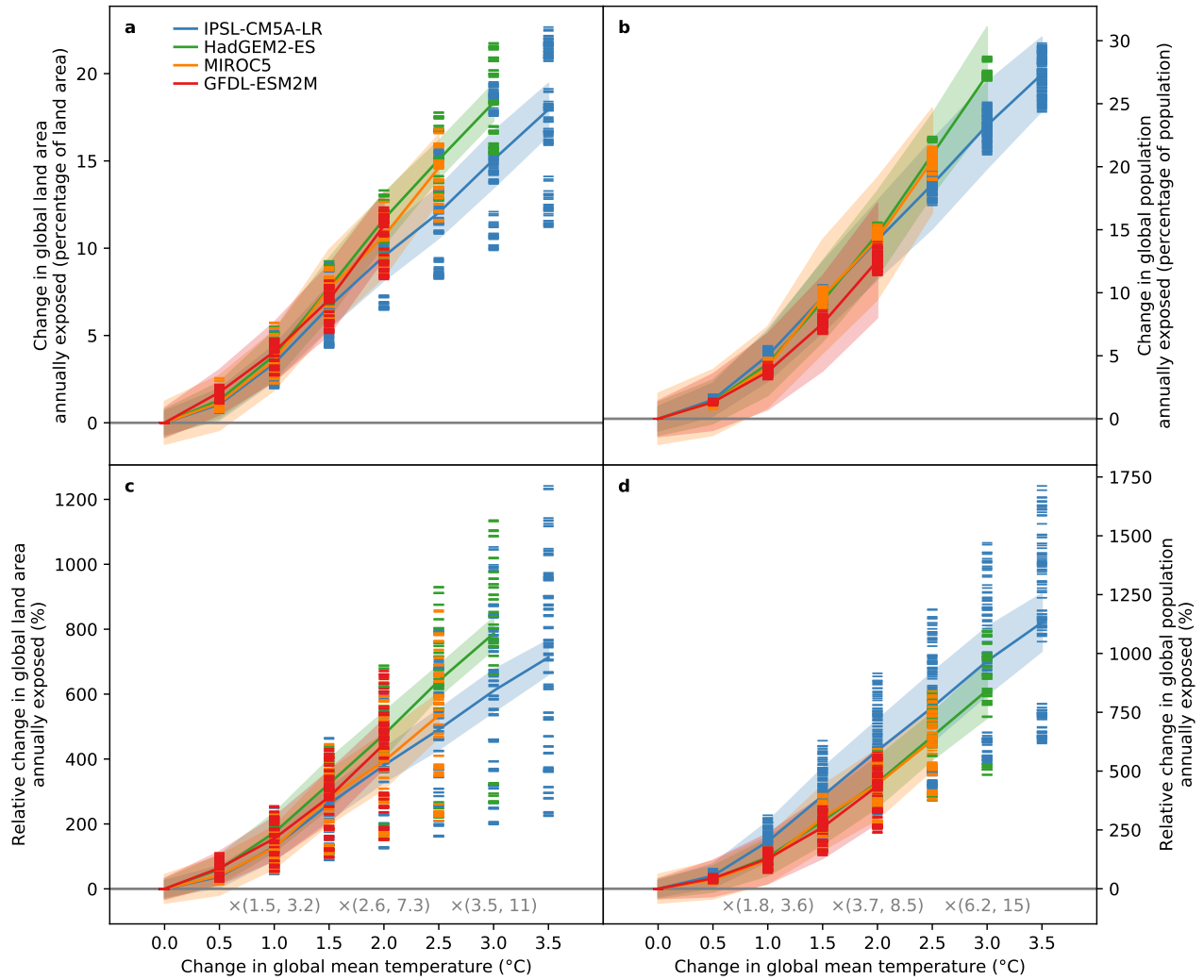


Figure S7. Pure effect of climate change on global (left) land area and (right) population annually exposed to extreme events from all six event categories combined. Shown are (top) changes and (bottom) relative changes in global exposure at different levels of global mean temperature change relative to the preindustrial baseline. Bars indicate multi-year mean changes for each GCM (color) and impact model combination. Lines represent medians over all impact model combinations per GCM. Shaded areas represent the multi-impact-model median of the multi-year mean change in exposure \pm the multi-impact-model median of the interannual standard deviation of exposure. Grey numbers at the bottom of panels c–d indicate the central 90 % multi-model range of change factors at 1 °C, 2 °C, and 3 °C global warming relative to preindustrial conditions.

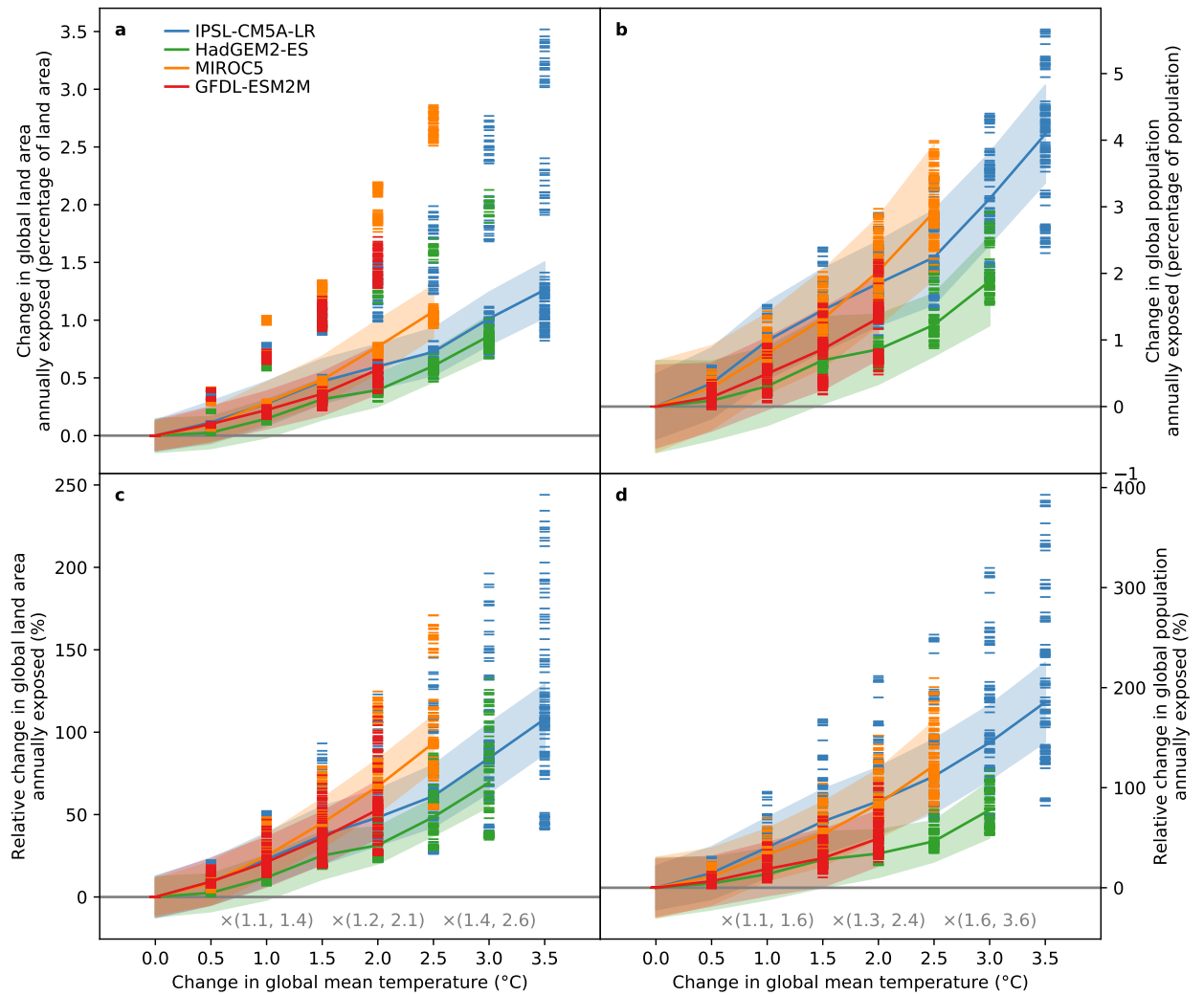


Figure S8. Same as Fig. S7 but for global exposure to confined events.

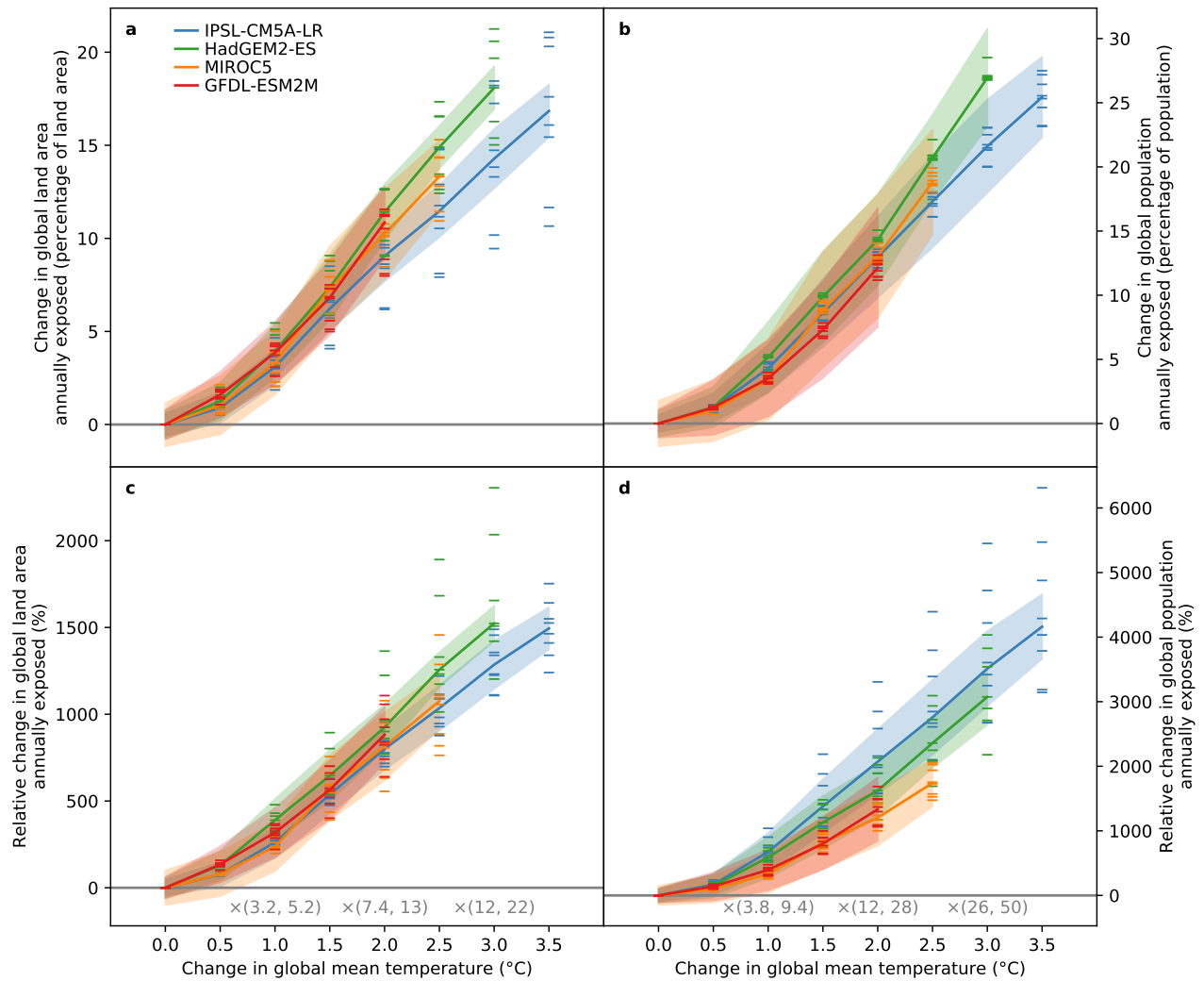


Figure S9. Same as Fig. S7 but for global exposure to extensive events.

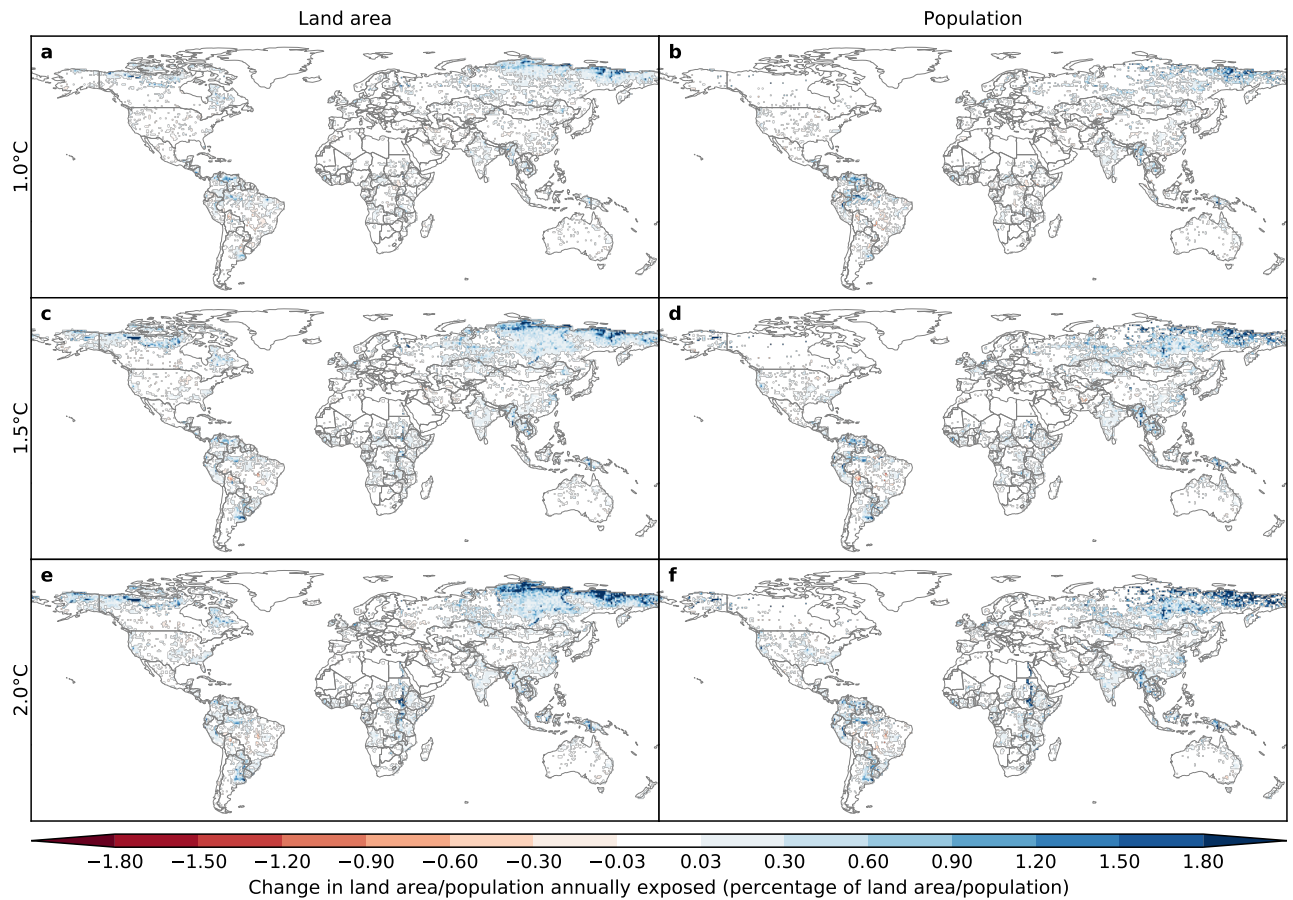


Figure S10. Change in (left) land area and (right) population annually exposed to river floods at the grid scale for (a, b) 1°C, (c, d) 1.5°C, and (e, f) 2°C global warming relative to preindustrial climate conditions. Changes are expressed as percentages of the land area or population of each $0.5^\circ \times 0.5^\circ$ grid cell. Colors indicate multi-model median changes in multi-year mean exposure. White indicates missing data over Greenland and a small change or less than 66% model agreement on the sign of the change elsewhere.

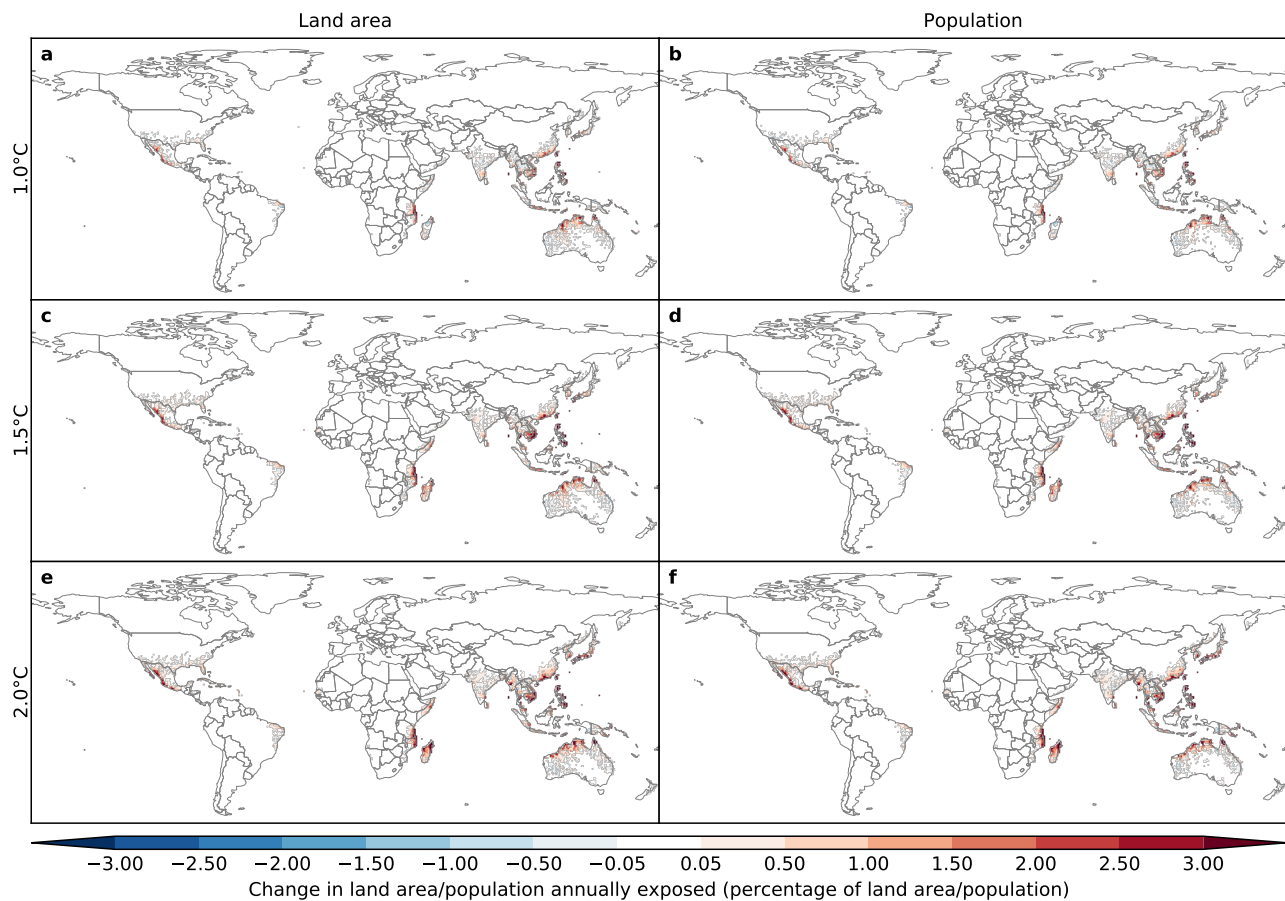


Figure S11. Same as Fig. S10 but for grid scale exposure to tropical cyclones.

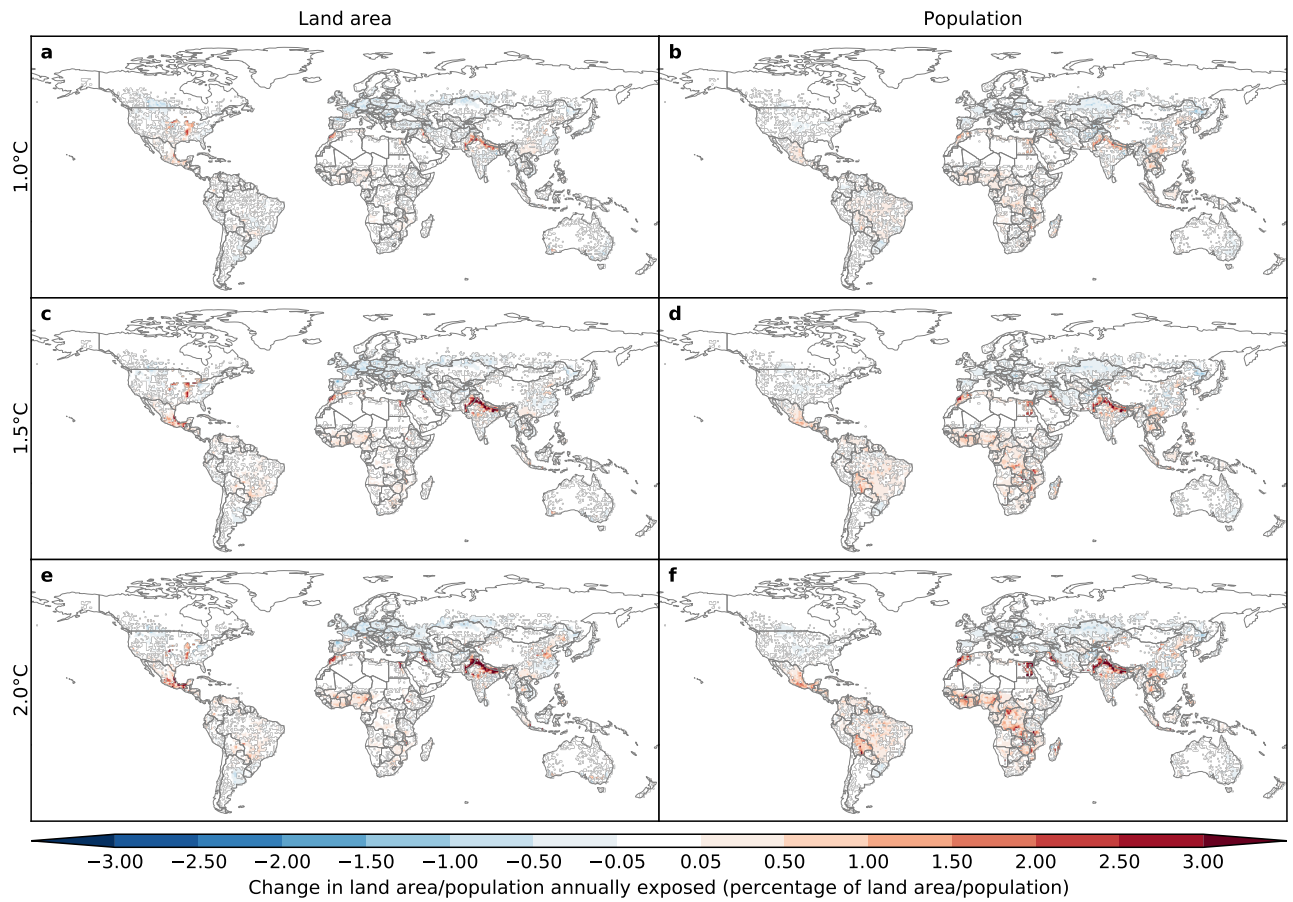


Figure S12. Same as Fig. S10 but for grid scale exposure to crop failure.

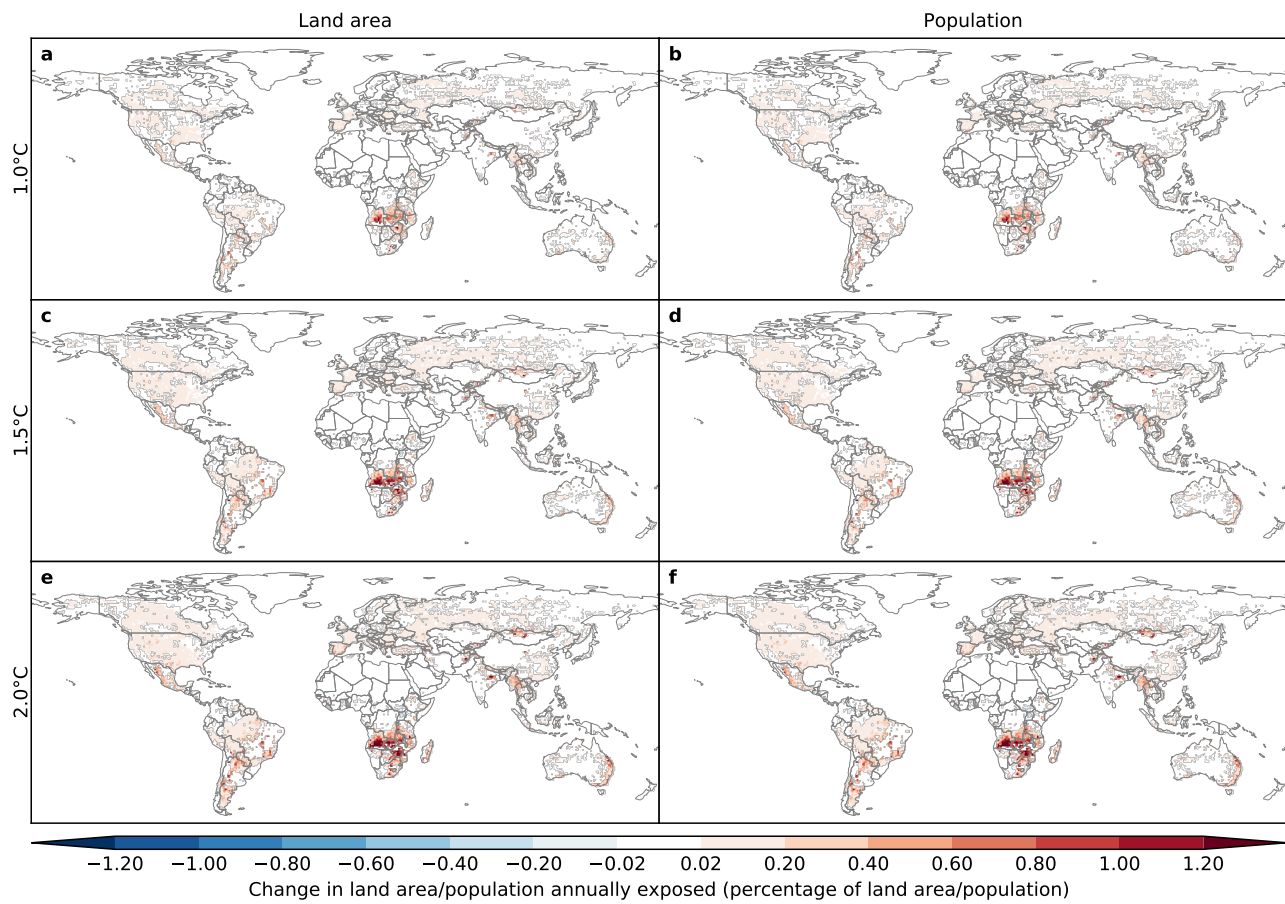


Figure S13. Same as Fig. S10 but for grid scale exposure to wildfire.

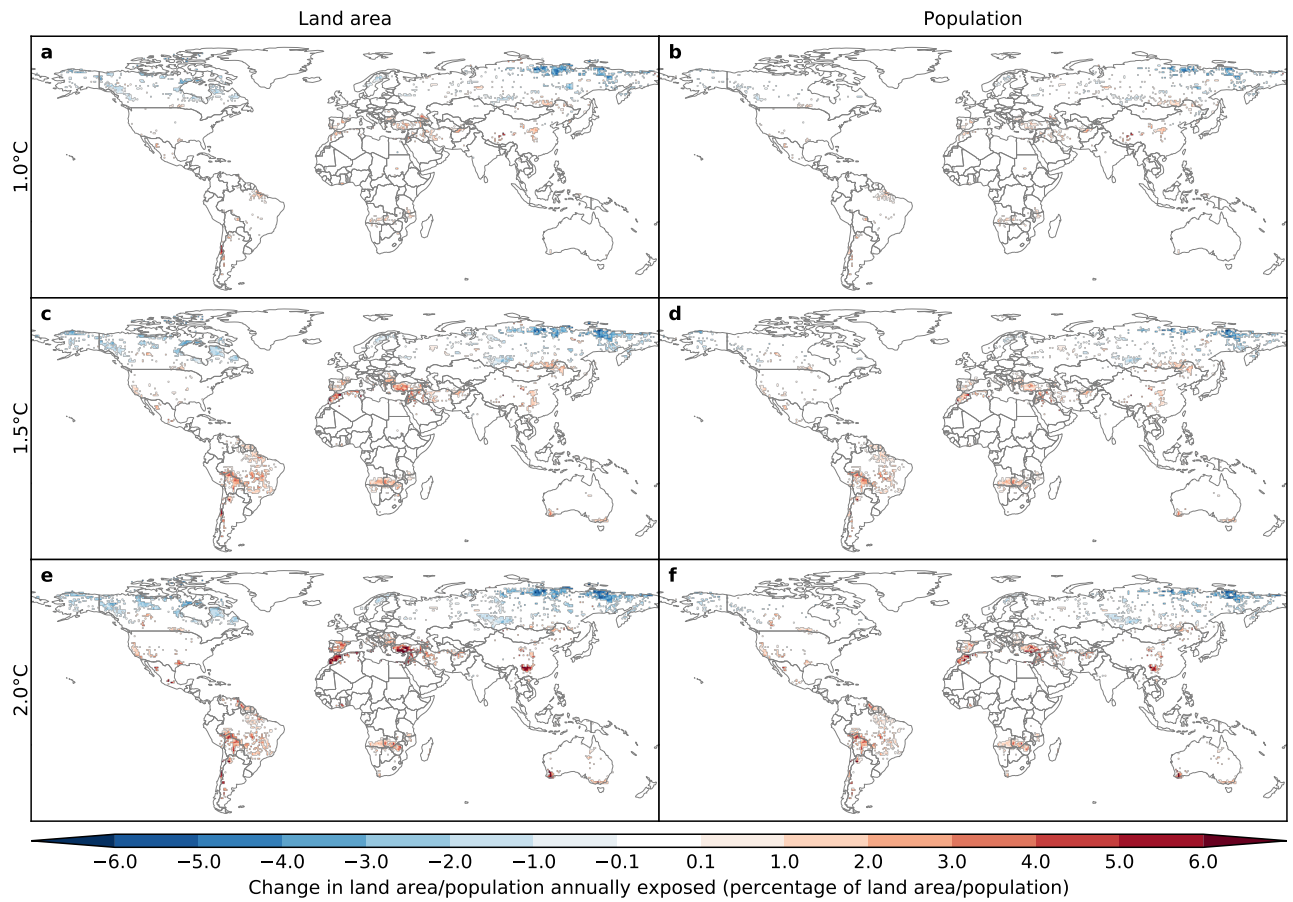


Figure S14. Same as Fig. S10 but for grid scale exposure to droughts.

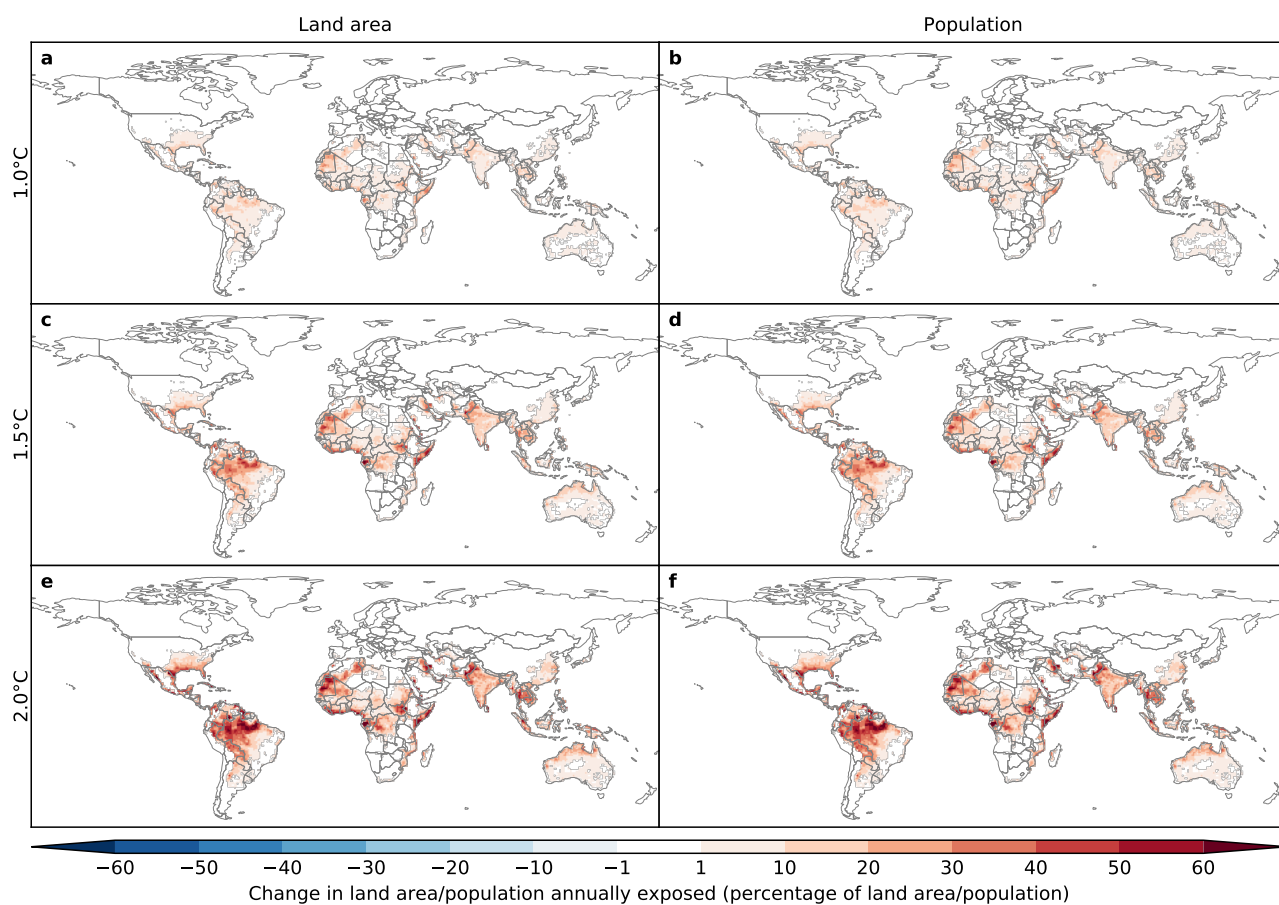


Figure S15. Same as Fig. S10 but for grid scale exposure to heatwaves.

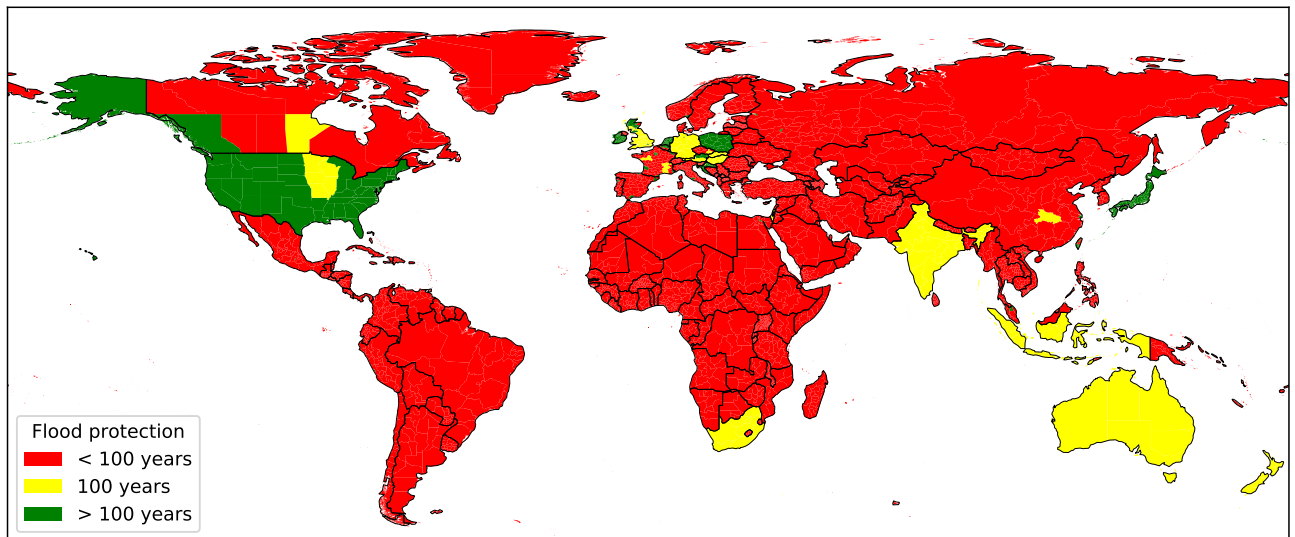


Figure S16. Estimated present day protection levels against river floods expressed in return levels of discharge based on the FLOPROS database (Scussolini et al., 2016). Red areas: Flood protection is lower than assumed here. Yellow areas: Flood protection corresponds to the protection level assumed here. Green areas: Flood protection exceeds the level of protection assumed here.

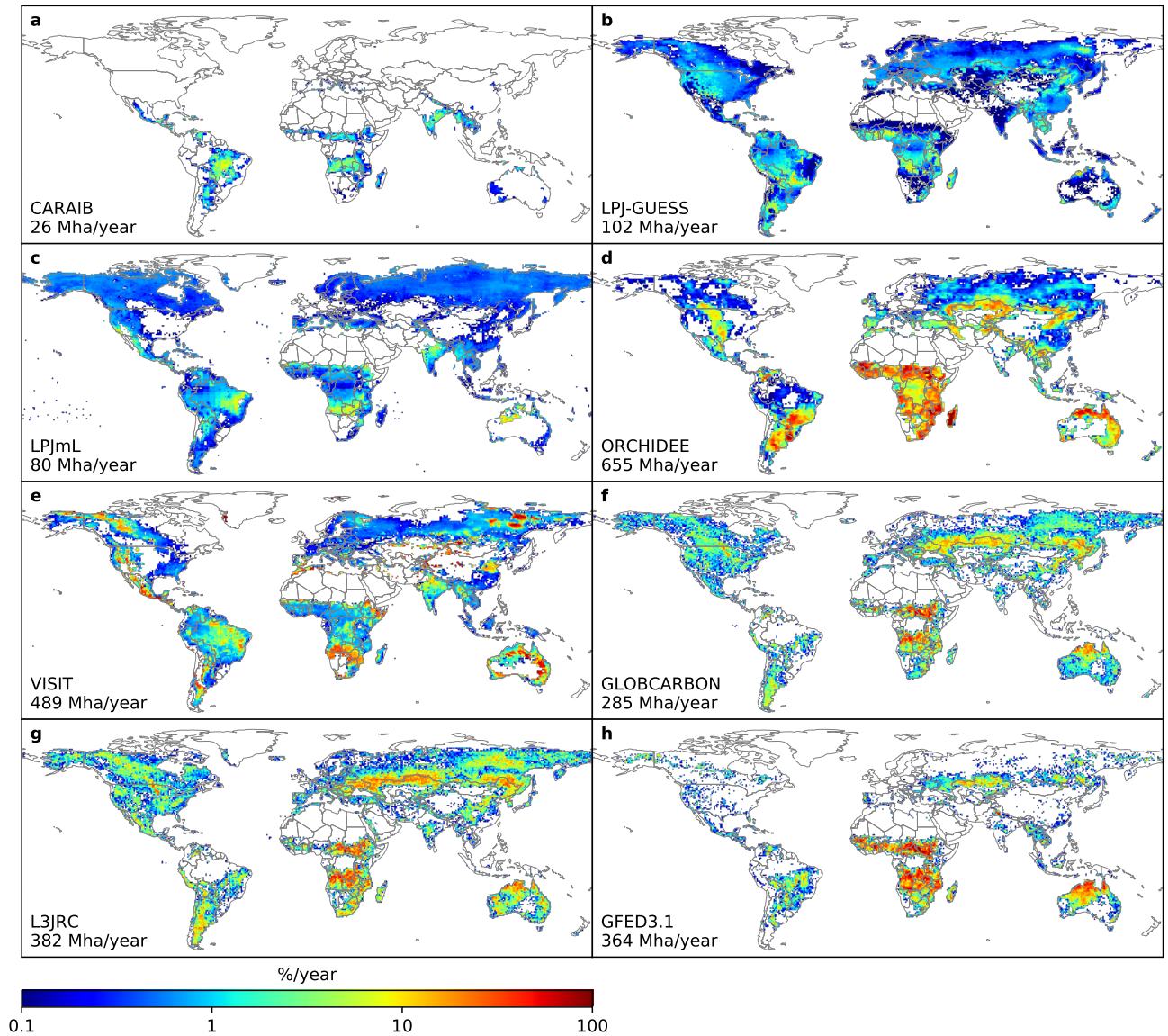


Figure S17. Mean annual burned area fraction at grid scale (color, in percent) and annual global burned area (annotated in the lower left corner of each panel) over 2001–2005 as simulated by (a) CARAIB, (b) LPJ-GUESS, (c) LPJmL, (d) ORCHIDEE, and (e) VISIT driven with IPSL-CM5A-LR historical climate input data, and as observed according to the satellite-derived burned area datasets (f) GLOBCARBON (Plummer et al., 2007), (g) L3JRC (Tansey et al., 2008) and (h) GFED3.1 (Giglio et al., 2010).

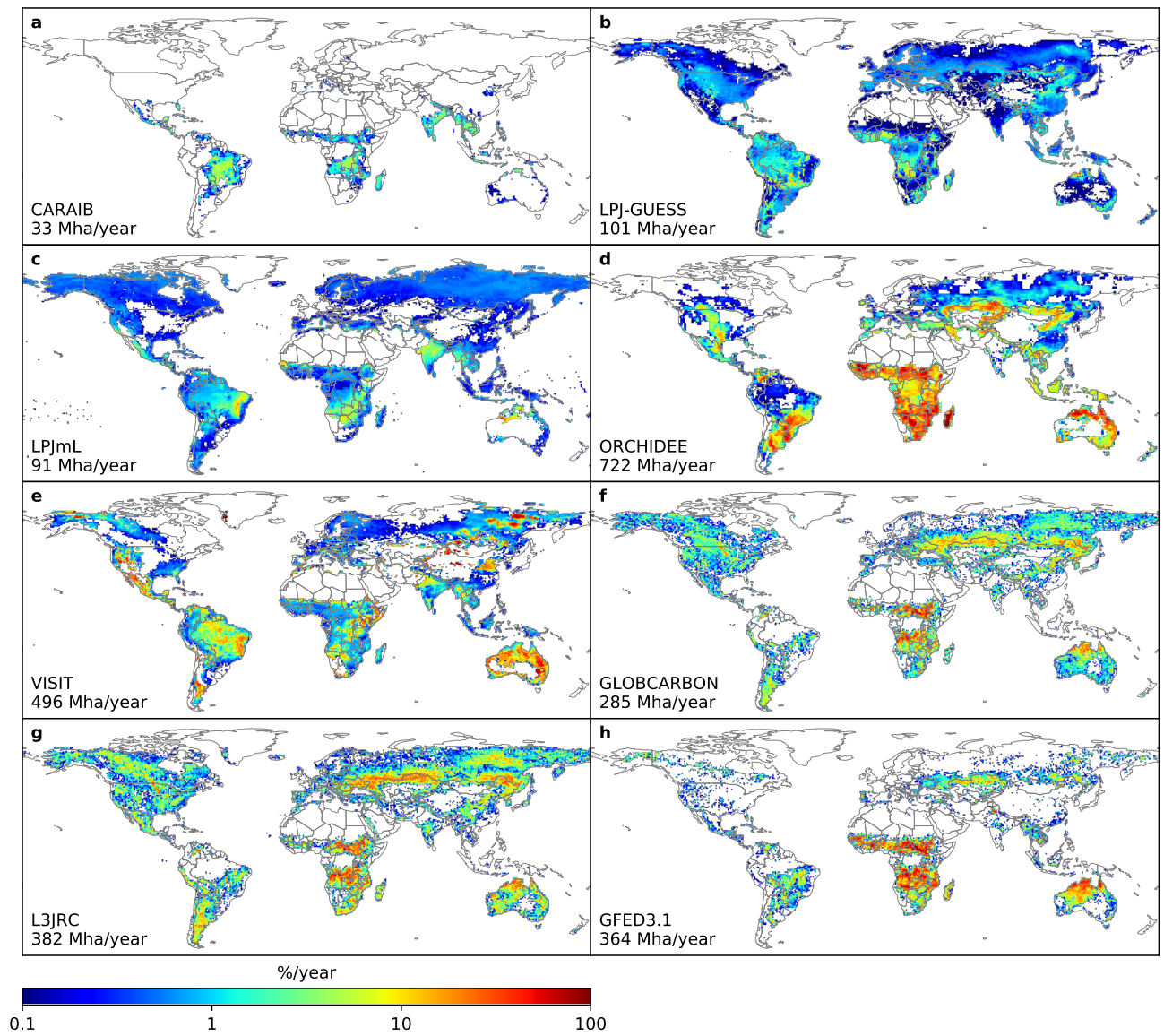


Figure S18. Same as Figure S17 but for GVMs driven with GFDL-ESM2M historical climate input data.

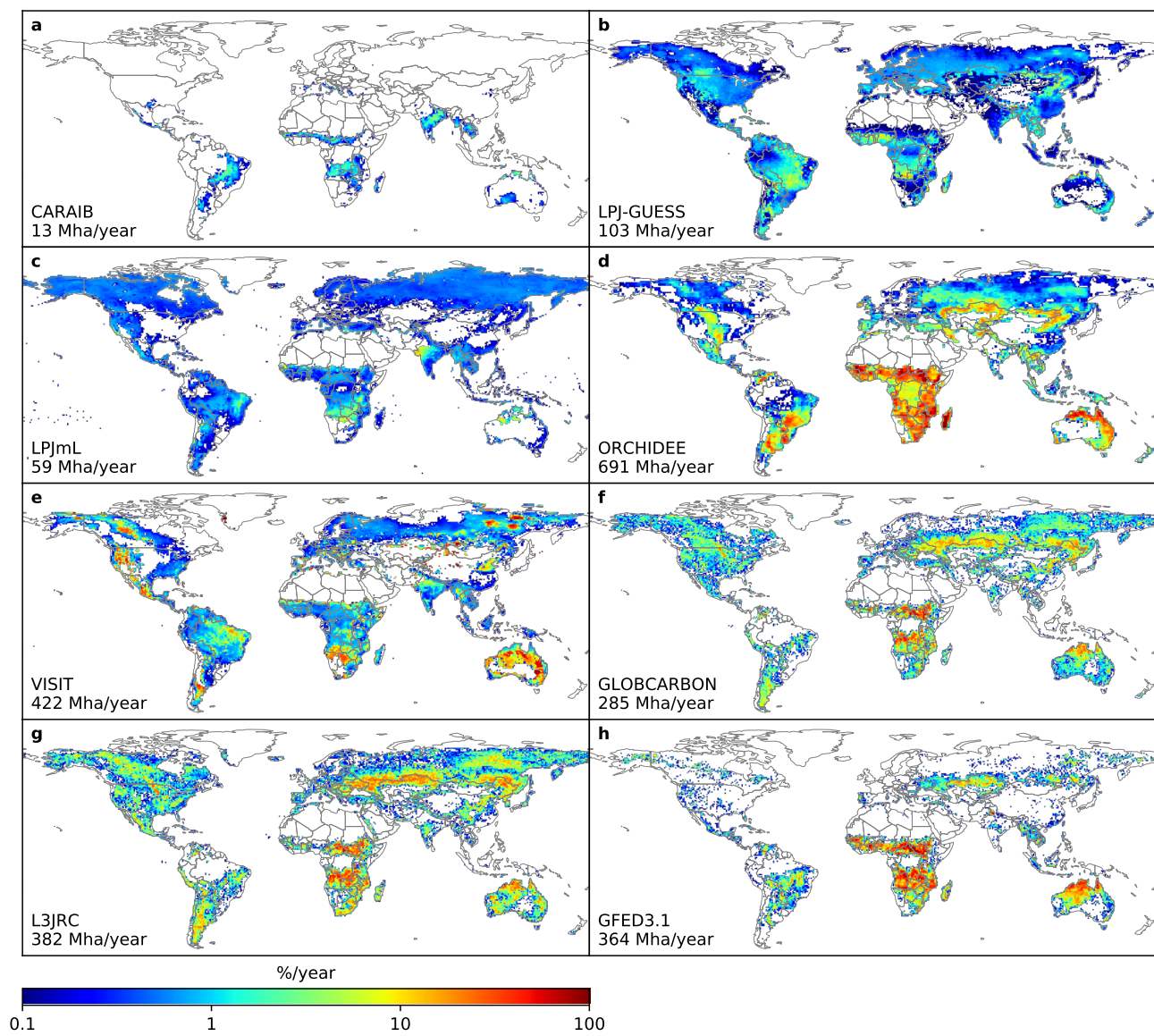


Figure S19. Same as Figure S17 but for GVMs driven with MIROC5 historical climate input data.

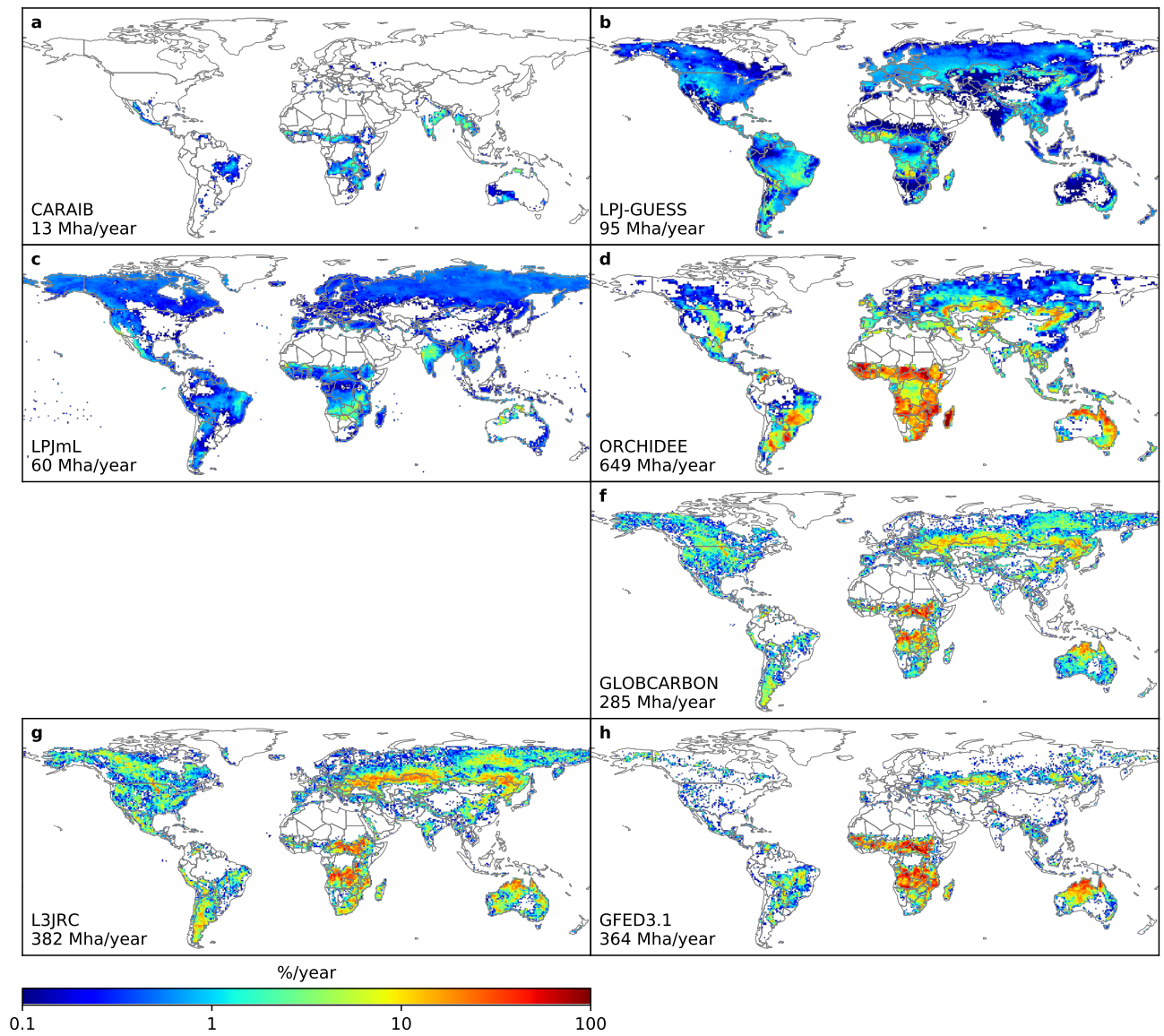


Figure S20. Same as Figure S17 but for GVMs driven with HadGEM2-ES historical climate input data.

Table S1. Main characteristics of the Global Hydrological Models (GHMs).

GHM	Energy balance	Soil scheme	Evaporation scheme	Runoff scheme	Snow scheme
CLM45 (Lawrence et al., 2011; Oleson et al., 2013)	Yes	15 soil layers with variable thickness down to 42 m	Monin-Obukhov similarity theory	Saturation excess, fractional area	Energy balance, up to 5 layers
H08 (Hanasaki et al., 2018)	Yes	1 soil layer with a depth of 1 m	Bulk formula	Saturation excess, non-linear	Energy balance
JULES-W1 (Best et al., 2011; Papadimitriou et al., 2017)	Yes	4 soil layers of 10, 25, 65 and 200 cm thickness	Penman-Monteith	Hortonian infiltration excess mechanism enhanced by vegetation specific factors	Energy balance
LPJmL (Rost et al., 2008; Schaphoff et al., 2013)	No	5 soil layers of 20, 30, 50, 100 and 100 cm thickness	Priestley-Taylor	Saturation excess	Degree Day
MPI-HM (Hagemann & Dümenil Gates, 2003; Stacke & Hagemann, 2012)	No	Prescribed by plant rooting depth	Penman-Monteith	Saturation excess, non-linear	Degree Day
PCR-GLOBWB (Wada et al., 2014, 2016)	No	2 soil layers of 0.3 and 1.2 m depth	Hamon	Saturation excess, beta function	Degree Day
ORCHIDEE (Guimberteau et al., 2014)	Yes	11 soil layers down to 2 m depth	Bulk formula	Infiltration excess	Energy balance
WaterGAP2 (Müller Schmied et al., 2014, 2016)	No	1 soil layer with varying depth of 0.1 to 4 m depending on land cover type	Priestley Taylor with two alpha factors	Saturation excess, beta function	Degree Day

Table S2. Basic global gridded crop model (GGCMs) characteristics. More detailed information on model setups is provided in Folberth et al. (2016) and Müller et al. (2017).

GGCM	CO ₂ fertilization	Representation of human management	Calibration
GEPIC (Liu, Yang, Folberth, et al., 2016; Liu, Yang, Liu, et al., 2016; Williams, 1995)	RUE, TE	Representation of nutrient constraints: N application based on HYDE3.2 (Klein Goldewijk et al., 2017) dataset provided within ISIMIP2b. 1/3 of total dose applied at planting, 2/3 about 40 days after germination. Implementation of growing seasons: Planting dates are based on the data provided within the global gridded crop model inter-comparison project (Elliott et al., 2015); total heat units to reach maturity remain constant over time but vary spatially according to reported growing seasons for the recent historic period. Winter and spring wheat are distributed according to Stehfest, Heistermann, Priess, Ojima, and Alcamo (2007): Winter wheat is planted in grid cells with a minimum temperature in the coldest month of the year of > −10 °C and < 5 °C based on decadal monthly means during the recent historic time period and kept constant over time.	The model is not calibrated explicitly but has been evaluated in detail (Folberth et al., 2012). Maize cultivars are distributed based on the human development index (HDI) with high-yielding cultivars in countries with HDI > 80 and low-yielding in all others. Soils were pre-conditioned in a spin-up run as described in Folberth et al. (2012). Subsequently, soils were treated statistically in the model with an annual re-initialization of all soil properties except soil humidity and mineral N.
LPJmL (Bondeau et al., 2007)	LLP, CC	Representation of nutrient constraints: Soil nutrient limiting factors are not accounted for. Implementation of growing seasons: Planting dates are based on the data provided within the global gridded crop model inter-comparison project (Elliott et al., 2015); total heat units to reach maturity remain constant over time but vary spatially according to reported growing seasons for the recent historic period.	Leaf Area Index, Harvest Index, and a scaling factor that scales leaf-level photosynthesis to stand level are adjusted to reproduce observed yields on country level (1996–2000).
PEPIC (Liu, Yang, Folberth, et al., 2016; Liu, Yang, Liu, et al., 2016; Williams, 1995)	RUE, TE	Representation of nutrient constraints: Flexible N application based on N stress > 10 % with a maximum value according to the ISIMIP2b input data; phosphorus deficiency not considered. Implementation of growing seasons: Fixed sowing dates (Sacks et al., 2010); potential heat units to reach maturity based on average growing season temperature between 1980 and 2010, i.e. they vary spatially but stay constant over time.	Model parameters are adjusted to reproduce average (1998–2002) reported yields (FAO) on national level.

Table S3. Main characteristics of fire modules of global vegetation models (GVMs).

GVM	Fire ignition factors	Human influence on fire ignition and/or suppression included	How is fire spread/extent modelled	Minimum Vegetation burned area fraction at grid level	Vegetation types allowed to burn besides natural vegetation
CARAIB (Dury et al., 2011)	availability of fuel, combustibility of fuel (soil moisture), presence of natural ignition source (lightning flash data)	no	function of soil moisture and wind speed	0	none
LPJmL (Thonicke et al., 2001; Bondeau et al., 2007; Schaphoff et al., 2013)	ignition occurs once soil moisture threshold for available litter associated with plant productivity is reached	no	empirical relationship between the length of the fire season and the annual area burned, where the length of the fire season is derived from the number of fires initialized in the considered year	0.001	none
LPJ-GUESS (Thonicke et al., 2001; Smith et al., 2014)	as in LPJmL	no	as in LPJmL	0.001	managed pastures, rangeland, cropland
ORCHIDEE (Thonicke et al., 2010; Yue et al., 2014, 2015)	ignitions from anthropogenic and lightning sources (lightening flash data) based on availability of fuel, combustibility of fuel (soil moisture), presence of ignition source	both human ignitions and suppressions are implicitly included in a single equation based on population density, only anthropogenic fires are suppressed	fire spread simulated as a function of fuel load, fuel compact status, fire intensity and wind speed; final fire extent is determined by an assumed mean fire size derived from fire spread rate and duration, and the number of effective ignitions	0	managed pastures, rangeland
VISIT (Ito & Oikawa, 2002; Ito & Inatomi, 2012)	natural ignition based on availability of fuel, combustibility of fuel (soil moisture)	no	fire extent is an empirical function of soil moisture and fuel load	0	managed pastures, rangeland

Table S4. Direct human influences (DHIs) considered in impact model simulations analysed in this study. The following abbreviations are used: hist, historical changes of DHIs considered up to 2005 and fixed at 2005 levels thereafter (histsoc and 2005soc according to ISIMIP2b protocol, respectively); fixed, DHIs considered fixed at 2005 levels (2005soc according to ISIMIP2b protocol); fixed*, DHIs considered fixed at levels representative of some recent historical period (see Table S2); NA, DHIs not considered.

Global hydro-logical model	land-use terns	pat- terns	irrigation pat- terns	domestic and industrial wa- ter use	livestock wa- ter use	dams and reservoirs	and
CLM4.5	fixed		fixed	NA	NA	NA	
H08	fixed		fixed	fixed	NA	fixed	
LPJmL	hist		hist	hist	NA	hist	
JULES-W1	fixed		NA	NA	NA	NA	
MPI-HM	hist		hist	NA	NA	NA	
ORCHIDEE	hist		hist	NA	NA	NA	
PCR- GLOBWB	hist		hist	hist	hist	hist	
WaterGAP2	fixed		hist	hist	hist	hist	
Global vegeta- tion model	land-use terns	pat- terns	irrigation pat- terns	influence on fire ignition and suppression			
CARAIB	hist		NA	NA			
LPJ-GUESS	hist		NA	NA			
LPJmL	hist		hist	NA			
ORCHIDEE	hist		hist	hist			
VISIT	hist		NA	NA			
Global ded model	grid- crop	land-use terns	pat- terns	irrigation pat- terns	cultivars	sowing dates	fertilizer input
GEPIC		hist		hist	fixed*	fixed*	fixed
LPJmL		hist		hist	fixed*	fixed*	NA
PEPIC		hist		hist	fixed*	fixed*	fixed

Table S5. GCM-specific number of simulation years from CMIP5 experiments historical, RCP2.6, and RCP6.0 per global warming level bin.

ΔT bin ($^{\circ}\text{C}$)	IPSL-CM5A-LR	HadGEM2-ES	MIROC5	GFDL-ESM2M
$[-0.5, 0.0[$	18	65	47	36
$[0.0, 0.5[$	82	71	84	96
$[0.5, 1.0[$	33	19	51	38
$[1.0, 1.5[$	23	93	228	119
$[1.5, 2.0[$	121	230	96	20
$[2.0, 2.5[$	201	16	19	24
$[2.5, 3.0[$	25	12	8	0
$[3.0, 3.5[$	18	18	0	0
$[3.5, 4.0[$	11	6	0	0
$[4.0, 4.5[$	1	0	0	0